Geol. Mag. **149** (*1*), *2012, pp. 39–55.* © *Cambridge University Press 2011*
doi:10.1017/S0016756811000173

Triassic shoshonitic dykes from the northern North China craton: petrogenesis and geodynamic significance

LEBING FU*†, JUNHAO WEI*, TIMOTHY M. KUSKY‡, HUAYONG CHEN§, JUN TAN*, YANJUN LI*, LINGJUN KONG* & YONGJIAN JIANG*

*Faculty of Earth Resources, China University of Geosciences, Wuhan 430074, China
‡State Key Laboratory of Geological Processes and Mineral Resources, Three Gorges Geohazard Research Centre, China University of Geosciences, Wuhan 430074, China
§ARC Centre of Excellence in Ore Deposits, University of Tasmania, Tasmania 7001, Australia

(*Received* 30 March 2010; *accepted* 5 January 2011; *first published online* 9 March 2011)

Abstract – Zircon U–Pb ages, major and trace element geochemistry and Sr, Nd and Pb isotope compositions of diorite and diorite porphyry dykes from the Jinchanggouliang (JCGL) gold ore field on the northern margin of the North China craton (NCC) were studied to investigate their sources, petrogenesis and geodynamic significance. LA-ICP-MS zircon U–Pb dating reveals three major age groups of 2500 Ma (n = 2), 253 ± 7 Ma (n = 5) and 227 ± 1 Ma (n = 9). The inherited ages of 2500 Ma, contemporary with the Archaean NCC continental growth, imply that crustal material was involved in the magma source. The igneous zircons with a concordia age of 227 ± 1 Ma may record the emplacement age of the JCGL dykes. Both diorite and diorite porphyry exhibit a wide range of SiO_2 and MgO contents and are characterized by high concentrations of Na_2O+K_2O and Al_2O_3, and low abundances of P_2O_5 and TiO_2. They are enriched in large ion lithophile elements and light rare earth elements without significant Eu anomalies, and depleted in high-field-strength elements; all are categorized as shoshonitic rocks. All samples show a narrow range of Sr isotope compositions with initial $^{87}Sr/^{86}Sr$ ratios from 0.70394 to 0.70592, variable $\varepsilon_{Nd}(t)$ values (1.1 to −12.0) and T_{DM2} ages of 913–1972 Ma. Their Pb isotope compositions form continuous variation trends and plot in the fields between enriched mantle 1 (EM1) and lower continental crust (LCC). The above results suggest that the JCGL dykes studied could have been derived from mixing of lower crust, lithospheric mantle of the NCC and ascending asthenospheric melt in a post-orogenic extensional geodynamic setting. These shoshonitic dykes, together with the geochronological data of regional ENE-trending retrograded eclogites, ophiolites, continental arc magmatic belt, A-type granite, alkaline intrusions and metamorphic core complex from the northern NCC and Central Asian Orogenic Belt (CAOB) suggest that closure of the Palaeo-Asian Ocean (i.e. stage of pre-collision to collision) had completed during latest Permian to earliest Triassic time, and that the CAOB was subsequently tectonically dominated by post-orogenic extensional regimes. The involvement of asthenospheric melt in the magma source implies that the sub-continental lithospheric mantle (SCLM) of the NCC had been modified, and the onset of lithospheric destruction and thinning beneath the northern NCC may have occurred in Middle–Late Triassic time as a result of post-orogenic subducting slab detachment and lithospheric delamination.

Keywords: dyke, post-orogenic extension, delamination, lithosphere destruction, Central Asian Orogenic Belt, Jinchanggouliang.

1. Introduction

High-K calc-alkaline to shoshonitic dykes are widespread in various tectonic settings such as continental arcs, post-collisional arcs and within-plate setting (Müller, Rock & Groves, 1992; Scarrow *et al.* 1998). The orientation of individual dykes can reflect the stress field at the time of intrusion (Vaughan, 1996; Hou *et al.* 2006), and the dyke swarms may provide important information about the tectonic evolution of orogenic belts (Yang *et al.* 2004; Luo *et al.* 2006). Moreover, they can be used to identify magma source compositions (Adams *et al.* 2005; Xu *et al.* 2007) and evolutionary history (Chistyakova & Latypov, 2008; Mayborn, Lesher & Connelly, 2008). Nevertheless, the petrogenesis of these dykes is complex and diverse. They were generally thought to be formed by (1) continental crust contamination of mafic magmas (Currie & Williams, 1993), (2) partial melting of enriched lithospheric mantle either in a subduction-related environment (Tan *et al.* 2007; Liu *et al.* 2008*a*) or in the sub-continental lithospheric mantle (SCLM) (Canning *et al.* 1996; Chen & Zhai, 2003), (3) mixing of upwelling basaltic magma with the ultrapotassic lithospheric-mantle melt caused by heating and/or thinning of SCLM (Thompson *et al.* 1990; Xu *et al.* 2007), or mixing of mantle-derived basaltic or lamproitic melts and crust-derived silicic melts (Prelevic *et al.* 2004; Tan *et al.* 2008).

Owing to their important geodynamic and petrogenetic significance, we studied the Jinchanggouliang (JCGL) diorite and diorite porphyry dykes. The JCGL

†Author for correspondence: fulebing1212@126.com

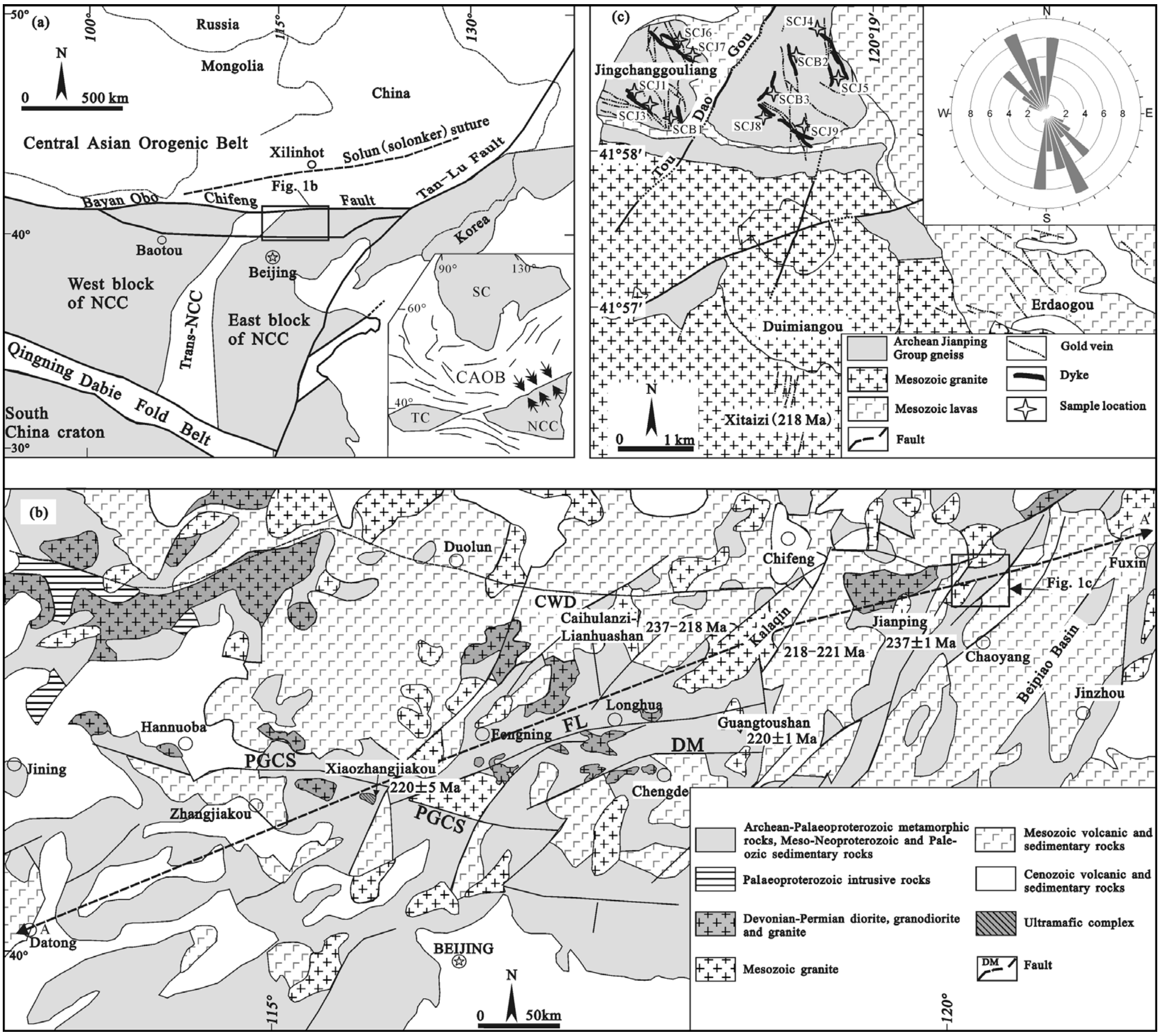

Figure 1. (a) Tectonic setting of the northern margin of the NCC and location of Figure 1b (modified after Zhao *et al.* 2001; Hart *et al.* 2002; Zhang *et al.* 2008*b*). The inset shows the major tectonic units of north Asia and arrows denote the principal stress direction of the NCC during latest Permian to earliest Triassic time (Wan, 2004; Hou, Wang & Hari, 2010). TC – Tarim craton; NCC – North China craton; SC – Siberia craton; CAOB – Central Asian Orogenic Belt. (b) Geological sketch of the central-eastern segment of the northern margin of the NCC (modified after Zhang *et al.* 2007) showing the location of A–A′ cross-section illustrated in Figure 11. Geochronology data for the Jianping syenogranite dyke and monzogranite (Zhang *et al.* 2009*c*), Kalaqin (also called Harqin) diorite (Shao *et al.* 2000), Caihulanzi–Lianhuashan diorite (She *et al.* 2000; Han, Shao & Zhou, 2000), Guangtoushan alkaline granite (Han, Kagami & Li, 2004) and Xiaozhangjiakou ultramafic complex (Tian *et al.* 2007) are also presented. Fault names: CWD – Chifeng–Weichang–Duolun fault; PGCS – Pingquan–Gubeikou–Chicheng–Shangyi fault; FL – Fengning–Longhua fault; DM – Damiao fault. (c) Detailed geological map of the Jinchanggouliang–Erdaogou area. The inset illustrates strike rose diagram of dykes (n = 42).

occupies a transitional tectonic position that links the Phanerozoic Central Asian Orogenic Belt (CAOB) in the north, with the Precambrian North China craton (NCC) in the south (Fig. 1a). The CAOB is one of the world's largest sites of juvenile crustal formation in the Phanerozoic (Xiao *et al.* 2003; Windley *et al.* 2007), and it formed with the final closure of Palaeo-Asian Ocean and amalgamation of the NCC and the Mongolian arc terranes, which both took place along the Solonker suture zone (Fig. 1a; Davis *et al.* 2001; Xiao *et al.* 2003). However, there is still much controversy concerning the timing of suturing. Some authors propose that the suturing took place during Late Permian to Early Triassic time (Chen *et al.* 2000; Davis *et al.* 2001; Xiao *et al.* 2003); whereas others prefer suturing during either Middle Devonian time (Tang, 1990; Xu & Chen, 1997) or Late Devonian–Early Carboniferous time (Shao, 1991; Hong *et al.* 1995). Additionally, the NCC is regarded as a Precambrian craton that experienced widespread tectonothermal reactivation (lithosphere destruction and thinning) (e.g. Gao *et al.* 2002; Rudnick *et al.* 2004; Kusky, Windley & Zhai, 2007*a*,*b*), but the initiation timing for reactivation is still controversial (Wu *et al.* 2008; Xu *et al.* 2009). Although most researchers believe that the destruction of the NCC occurred during late Mesozoic time (e.g. Zhang *et al.* 2002; Menzies *et al.* 2007), other researchers proposed that the destruction probably began in early Mesozoic time (e.g. Han, Kagami & Li, 2004). In a recent paper by Zhang *et al*. (2009*b*), it is proposed that the lithospheric destruction and thinning of the northern NCC began in Middle–Late Triassic time.

In this paper, we present zircon U–Pb ages, major and trace element geochemistry, and Sr–Nd–Pb isotope compositions for the Triassic dykes from JCGL to (1) document the geochronology and geochemical characteristics of these rocks, (2) investigate their magma sources and petrogenesis and (3) evaluate the evolution of the CAOB and its influence on the early Mesozoic lithospheric mantle beneath the NCC.

2. Geological setting

The CAOB is located between the North China and Siberian cratons (Fig. 1a). It is a complex orogenic belt formed through successive accretion of arc complexes, accompanied by emplacement of voluminous subduction-related granitic magmas mainly during Palaeozoic times (e.g. Davis *et al*. 2001; Xiao *et al*. 2003; Windley *et al*. 2007; Chen, Jahn & Tian, 2009) and closure of the Palaeo-Asian Ocean. In this period, multiple Mongolian arc terranes were amalgamated to the active margins of the NCC (Davis *et al*. 2001; Zhang *et al*. 2009*c*). The Solonker suture marks the location of the final closure of the Palaeo-Asian Ocean and the collision between the NCC and Mongolian composite terranes (e.g. Davis *et al*. 2001; Xiao *et al*. 2003; Windley *et al*. 2007; Miao *et al*. 2008). With the exhaustion of the Palaeo-Asian Ocean, the NCC and the southern Mongolian terranes were amalgamated and behaved as a combined North China–Mongolian plate (Davis *et al*. 2001).

The basement of the NCC is composed of highly metamorphosed Archaean and Palaeoproterozoic rocks that have been covered by Mesoproterozoic–Triassic marine and fluvial sediments, Jurassic–Cretaceous and younger sediments and volcanic rocks. According to the chronology, lithological assemblage, tectonic evolution and *P–T–t* paths, the NCC can be divided into the Eastern Block, the Western Block and the Trans-North China Orogen (Fig. 1a; Zhao *et al*. 2001). The presence of ≥3.6 Ga crustal remnants exposed on the surface and in lower crustal xenoliths in the NCC suggests that it has remained partially stable since the Early Archaean (Liu *et al*. 1992; Zheng *et al*. 2004*a*). The NCC experienced widespread lithospheric destruction and thinning after Palaeozoic times as indicated by the emplacement of voluminous late Mesozoic to Tertiary granites and alkali basalts (e.g. Gao *et al*. 2002; Zhang *et al*. 2002; Rudnick *et al*. 2004; Kusky, Windley & Zhai, 2007*b*).

The JCGL gold ore field lies on the northern margin of the NCC (Fig. 1b), southeast of the CAOB. It consists of three gold deposits, including the JCGL, Erdaogou and Changgaogou. The Mesozoic Xitaizi S-type granite (218 ± 4 Ma; Miao *et al*. 2003) and Duimiangou I-type granite (131–125 Ma; Wang, Xu & Yang, 1989; Lin *et al*. 1993) intruded the Archaean Jianping Group gneiss, which is also the country rock for the Au orebodies and dykes. Jurassic volcanic rocks crop out in the northeast corner of this gold district (Fig. 1c).

3. Petrography

All dyke samples were collected from underground between the +620 m and +460 m levels beneath the JCGL deposit and adjacent areas to avoid the effects of weathering on the surface. Sample locations were projected to the surface and are illustrated in Figure 1c. Sample GSJ2 used for zircon U–Pb dating was collected from the drift adjacent to the no. 15 lode at the +580 m level. There are tens of dykes cropping out in the JCGL ore field. Individual dykes mostly strike 320° NW to 10° NE (Fig. 1c) with dip angles of about 75° E–80° E. The prevailing orientations of dyke strikes, as illustrated in the rose diagram in Figure 1c, are nearly the same as those of the maximum principal compressive stress in the NCC during latest Permian to earliest Triassic time (160°–178°; Wan, 2004; Hou, Wang & Hari, 2010), which is also orthogonal to the collisional belt between the NCC and Mongolian arc terranes (Fig. 1a). Dykes exhibit narrow chilled margins and range from 1 to 5 m in width and are tens of metres to about 1 kilometre in length. All dykes are cut by gold-bearing quartz veins and can be generally classified into diorite and diorite porphyry.

The diorites are medium- to fine-grained rocks with hypidiomorphic granular texture, showing clear intrusive relationships with the host gneiss. They mainly consist of plagioclase (40–60 %), amphibole (30–40 %), pyroxene (1–3 %) and biotite (0–5 %), with minor amounts of quartz, magnetite, zircon and apatite. The plagioclase generally forms subhedral laths, with occasional albite and carlsbad–albite combined twinning. They are partly altered to sericite, calcite and epidote. Amphibole, the most abundant mafic mineral, is subhedral to euhedral and locally slightly altered to calcite and chlorite.

Diorite porphyry is grey-black, and has a porphyritic texture containing 15–20 % phenocrysts by volume. The phenocrysts consist dominantly of long-pillared hornblende (3–8 %) and platy plagioclase (10–15 %) with minor biotite and clinopyroxene. Minerals in the groundmass are mainly composed of plagioclase (50–65 %) and hornblende (15–20 %). Accessory minerals include acicular apatite, magnetite and zircon. The hornblende and plagioclase are both partly altered to sericite and chlorite.

4. Analytical methods

4.a. Zircon U–Pb isotopic dating

Zircons were extracted from whole-rock samples using the standard technique of density and magnetic separation at the Laboratory of Langfang Regional Geological Survey Institute, Hebei Province. Following

https://doi.org/10.1017/S0016756811000173 Published online by Cambridge University Press

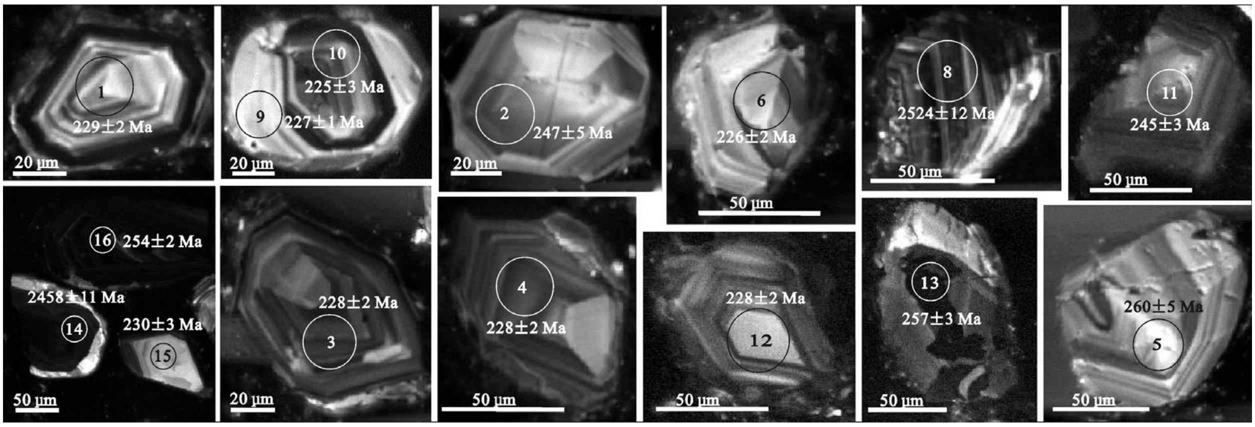

Figure 2. Cathodoluminescence images of zircons from sample GSJ2 showing sites of LA-ICP-MS U–Pb analyses.

this, the selected grains were mounted in epoxy blocks and carefully polished until their cores were exposed. The cathodoluminescence (CL) images, combined with reflected light and transmitted light, were obtained at the electron microprobe laboratory in the State Key Laboratory of Geological Processes and Mineral Resources (GPMR), China University of Geosciences, Wuhan, in order to observe the interior texture of the zircons. U–Pb isotopic analyses were made on a laser ablation inductively coupled plasma mass spectrometer (LA-ICP-MS, Agilent 7500a) with a spot size of 24 μm at GPMR following standard operating techniques as described by Liu *et al.* (2010). Common Pb was corrected using the method proposed by Anderson (2002). Concordia ages were determined using Isoplot 2.32 (Ludwig, 2003).

4.b. Major and trace element determination

Whole-rock samples were crushed in a corundum jaw crusher (to 60 mesh) and about 60 g was powdered in an agate ring mill to less than 200 mesh. Major element analyses were carried out at the Yichang Institute of Geology and Mineral Resources (YCIGM) in China by wet chemical methods with analytical errors less than 1.4 %. Trace elements were measured by an Agilent 7500a ICP-MS at GPMR. The samples were digested in Teflon bombs with a mixture of $HF+HNO_3$, as described by Liu *et al.* (2008*b*). Analyses of the international rock standards BHVO-1 and BCR-2 indicate that the analytical accuracy is mostly better than 10 % as indicated by the relative deviation.

4.c. Sr–Nd–Pb isotope analyses

Sr, Nd and Pb isotope compositions were measured on a Finnigan Mat 262 thermal ionization mass spectrometer at the YCIGM. Procedural blanks were 2.13×10^{-10} g for Sr, 2.13×10^{-10} g for Nd and 2×10^{-9} g for Pb. The working conditions of the instrument were controlled by international NBS-987 (Sr) and NBS-981 (Pb) standards and the laboratory ZK-bzNd (Nd) standard. The measured values for the NBS-987, NBS-981 and ZK-bzNd (Nd) standards were $^{87}Sr/^{86}Sr = 0.710246$, $^{207}Pb/^{206}Pb = 0.9142$ and $^{143}Nd/^{144}Nd = 0.511564$, respectively, during the period of data acquisition. $^{143}Nd/^{144}Nd$ values were corrected for mass fractionation by normalization to $^{146}Nd/^{144}Nd = 0.7219$, and $^{88}Sr/^{86}Sr$ ratios were normalized to $^{88}Sr/^{86}Sr = 8.3752$. The precision for $^{87}Rb/^{86}Sr$, $^{147}Sm/^{144}Nd$ and Pb are better than 1 %, 0.5 % and 0.033 %, respectively.

5. Analytical results

5.a. Zircon U–Pb geochronology

Zircons from sample GSJ2 are colourless to light yellow, transparent and dominated by short-, long-prismatic and equigranular shapes with a general length of 60–120 μm (Fig. 2). Sixteen spots on 13 zircon grains were measured and the analytical results are presented in Table 1. GSJ2–8 and GSJ2–14 yielded Archaean to Palaeoproterozoic inherited ages ($^{206}Pb/^{207}Pb$ age, 2524 ± 12 Ma and 2458 ± 11 Ma, respectively, Fig. 3b), which are consistent with an important continent growth period of the NCC (e.g. Zheng *et al.* 2004*b*; Kusky, Li & Santosh, 2007). The other 14 analyses are all concordant or almost concordant and fall into two distinct populations with a Late Permian to Early Triassic (GSJ2–2, GSJ2–5, GSJ2–11, GSJ2–13 and GSJ2–16) weighted mean of 253 ± 7 Ma (MSWD = 3.1, n = 5) and a Middle to Late Triassic weighted $^{206}Pb/^{238}U$ age mean of 227 ± 1 Ma (MSWD = 0.35, n = 9) (Fig. 3a). Irregularly oscillatory and fir leaf zoning from the former group (Fig. 2) indicate that they are inherited or captured. The latter group of zircons display obvious oscillatory zoning, higher Th/U ratios (0.50–0.98) and fall within a centralized area in the concordant diagram, so we interpret 227 ± 1 Ma as the emplacement time of the JCGL dykes.

5.b. Major and trace elements

Major and trace element data are listed in Table 2 and plotted in Figures 4–7. The JCGL dykes have a wide range of SiO_2 (51.22–68.48 wt %) and MgO

https://doi.org/10.1017/S0016756811000173 Published online by Cambridge University Press

Table 1. LA-ICP-MS zircon U–Pb dating data for dykes (GSJ2) from the JCGL

				U–Th–Pb isotopic ratios								Age (Ma)							
spot	Th ppm	U ppm	Th/U	$^{207}Pb/^{206}Pb$	1σ	$^{207}Pb/^{235}U$	1σ	$^{206}Pb/^{238}U$	1σ	$^{208}Pb/^{232}Th$	1σ	$^{207}Pb/^{206}Pb$	1σ	$^{207}Pb/^{235}U$	1σ	$^{206}Pb/^{238}U$	1σ	$^{208}Pb/^{232}Th$	1σ
GSJ2–01	321.86	359.17	0.90	0.05324	0.00149	0.26456	0.00914	0.03616	0.00035	0.01481	0.00021	339	63	238	7	229	2	297	4
GSJ2–02	164.66	178.22	0.92	0.05901	0.00780	0.31432	0.04053	0.03911	0.00085	0.01644	0.00066	567	291	278	31	247	5	330	13
GSJ2–03	392.37	509.97	0.77	0.05387	0.00135	0.26806	0.00797	0.03602	0.00035	0.01336	0.00054	366	57	241	6	228	2	268	11
GSJ2–04	294.71	301.86	0.98	0.05438	0.00168	0.27132	0.00895	0.03606	0.00037	0.01357	0.00025	387	69	244	7	228	2	272	5
GSJ2–05	118.28	269.26	0.44	0.05300	0.00351	0.29822	0.01922	0.04114	0.00075	0.01598	0.00079	329	151	265	15	260	5	320	16
GSJ2–06	152.51	212.31	0.72	0.05371	0.00183	0.26337	0.00868	0.03575	0.00036	0.01204	0.00025	359	77	237	7	226	2	242	5
GSJ2–07	141.06	179.76	0.78	0.05257	0.00193	0.26030	0.01002	0.03589	0.00043	0.01170	0.00026	310	84	235	8	227	3	235	5
GSJ2–08	370.55	611.77	0.61	0.16667	0.00121	9.34713	0.14692	0.40467	0.00306	0.11640	0.00128	2524	12	2373	14	2191	14	2226	23
GSJ2–09	372.52	452.29	0.82	0.05140	0.00108	0.25546	0.00716	0.03592	0.00030	0.01094	0.00014	259	48	231	6	227	2	220	3
GSJ2–10	155.28	258.61	0.60	0.05556	0.00210	0.27242	0.01231	0.03556	0.00048	0.01199	0.00028	435	84	245	10	225	3	241	6
GSJ2–11	181.04	272.41	0.66	0.05907	0.00213	0.31572	0.01419	0.03872	0.00051	0.01469	0.00036	569	79	279	11	245	3	295	7
GSJ2–12	149.67	249.27	0.60	0.04986	0.00160	0.24680	0.00957	0.03603	0.00035	0.01091	0.00022	189	75	224	8	228	2	219	4
GSJ2–13	205.00	999.49	0.21	0.05345	0.00097	0.29964	0.00823	0.04062	0.00045	0.01630	0.00039	348	41	266	6	257	3	327	8
GSJ2–14	77.34	1086.03	0.07	0.16027	0.00104	9.36261	0.19901	0.42142	0.00310	0.11894	0.00181	2458	11	2374	20	2267	14	2272	33
GSJ2–15	46.75	93.03	0.50	0.05216	0.00300	0.26160	0.01576	0.03633	0.00050	0.01239	0.00043	292	132	236	13	230	3	249	9
GSJ2–16	539.26	1707.27	0.32	0.05154	0.00072	0.28682	0.00718	0.04019	0.00029	0.01384	0.00017	265	32	256	6	254	2	278	3

(1.35–8.13 wt %) contents, with Mg numbers of 39–69. In addition, they are all characterized by high concentrations of Na_2O+K_2O (5.16–8.28 wt %) and Al_2O_3 (13.67–17.50 wt %) and low abundances of P_2O_5 (0.13–0.37 wt %) and TiO_2 (0.51–1.16 wt %). In the total alkali versus silica plot (not shown), samples mainly plot in the intersection field of basaltic-trachyandesite, trachyandesite, basaltic-andesite and andesite, which coincides with the classification results in terms of trace elements (Fig. 4). The linear arrays in the major element variation diagrams (Fig. 5a–d) indicate that the JCGL dykes may have resulted from magma mixing.

These dykes are enriched in large-ion lithophile elements (LILE, such as K, Rb, Sr and Ba), depleted in high-field-strength elements (HFSE, such as Nb, Ta and Ti) and have a range of concentrations of Cr and Ni (Fig. 5e, f). In the primitive mantle-normalized spider diagram, they display strong negative anomalies of Ta and Nb and positive Pb anomalies (Fig. 6a). All samples belong to the shoshonitic rock series according to the Ce/Yb–Ta/Yb and Th/Yb–Ta/Yb diagrams (Fig. 7). Samples exhibit sub-parallel right-dipping chondrite-normalized rare earth element (REE) patterns with $\sum$REE of 67.42–203.41 ppm (Fig. 6b). They may have experienced moderate fractionation characterized by $(La/Yb)_N$ values of 3.15–4.74. There is no clearly defined Eu anomaly (Eu/Eu* 0.72–1.13).

The major and trace element characteristics of the JCGL dykes are the same as those of the early Mesozoic Kalaqin diorite (Figs 1b, 6; Shao, Han & Li, 2000), which is also the host rock of the Caihulanzi (CHLZ) granulite xenoliths (Shao, Han & Li, 2000; She *et al.* 2006) and cumulate (Shao *et al.* 1999, 2000).

5.c. Sr–Nd–Pb isotopes

Sr, Nd and Pb isotope compositions are listed in Table 3. The JCGL dykes possess a narrow range of Sr isotope compositions with initial $^{87}Sr/^{86}Sr$ ratios of from 0.70394 to 0.70592, and variable $\varepsilon_{Nd}(t)$ values (1.1 to −12.0) and T_{DM2} ages (913–1972 Ma) (Fig. 8). Their Sr–Nd isotope compositions are nearly the same as those of the Mesozoic volcanic rocks from the transitional part of the CAOB and NCC (Zhou *et al.* 2001), and are different from the Palaeozoic lithospheric mantle and igneous rocks of the interior of the NCC or CAOB (Fig. 8a).

Pb isotope ratios of the JCGL dykes form continuous variation trends and plot between the fields of the enriched mantle 1 (EM1) and lower continental crust (LCC) in the Pb isotopic ratio plots ($(^{206}Pb/^{204}Pb)_i = 16.43$–$17.64$, $(^{207}Pb/^{204}Pb)_i = 15.21$–$15.56$, $(^{208}Pb/^{204}Pb)_i = 36.38$–$37.87$) (Fig. 9). Pb isotopic data for the Mesozoic Fangcheng basalts, which were thought to represent the late Mesozoic Pb isotopic signature of the enriched mantle beneath the NCC (Zhang *et al.* 2002), are shown in Figure 9 for reference.

https://doi.org/10.1017/S0016756811000173 Published online by Cambridge University Press

Table 2. Major (wt %) and trace element (ppm) compositions of dykes from the JCGL

Rock type	diorite							diorite porphyry									
Sample No.	SCJ1	SCJ3	SCJ4	SCJ5	J26–211-1*	Jc91–11-2*	Jc13–1*	SCJ6	SCJ7	SCJ8	SCJ9	SCB1	SCB2	SCB3	J26–13-5–2*	J26–711-3*	Jc91–4*
SiO_2	56.44	62.02	64.22	60.89	61.72	54.64	60.90	51.22	54.58	56.82	54.21	60.43	60.47	58.93	56.80	68.48	54.52
TiO2	1.04	0.83	0.80	0.89	0.51	0.81	0.55	0.83	0.87	0.84	0.85	0.62	0.64	0.65	1.16	0.51	1.06
Al_2O_3	16.87	15.21	14.92	15.67	15.43	15.00	15.17	15.00	15.36	15.11	15.16	13.82	13.88	13.67	16.69	14.73	17.50
Fe_2O_3	2.50	1.93	1.40	1.94	1.29	2.07	1.99	3.89	4.66	3.82	4.12	2.31	2.34	2.05	2.02	1.09	2.98
MnO	0.05	0.08	0.08	0.07	0.10	0.11	0.19	0.16	0.11	0.09	0.12	0.08	0.09	0.11	0.19	0.06	0.05
MgO	3.82	3.68	3.58	3.69	4.71	8.13	4.65	4.92	5.75	4.72	5.13	3.72	3.76	4.01	3.10	1.35	5.24
FeO	4.42	3.04	3.41	3.62	3.02	4.58	2.40	3.01	3.27	2.09	2.79	2.67	2.80	3.12	6.71	1.72	4.12
CaO	2.76	3.33	2.52	2.87	4.47	5.94	4.90	8.42	3.57	5.76	5.92	4.15	4.30	4.47	1.18	1.88	3.10
Na_2O	5.30	3.60	3.77	4.22	3.93	3.68	3.80	3.24	2.06	3.16	2.82	3.84	3.88	3.17	2.85	3.80	3.13
K_2O	2.59	2.80	2.66	2.68	1.95	1.79	1.73	2.93	3.10	2.96	3.00	3.23	3.29	3.80	4.98	4.18	5.15
P_2O_5	0.33	0.29	0.29	0.31	0.15	0.19	0.13	0.37	0.37	0.36	0.36	0.19	0.18	0.18	0.29	0.13	0.33
LOI	2.80	2.03	1.83	2.22	2.03	2.04	2.91	5.30	5.89	3.62	4.94	4.08	3.77	5.09	3.25	1.42	2.96
Total	98.93	98.84	99.47	99.08	99.31	98.98	99.32	99.29	99.59	99.35	99.41	99.13	99.40	99.25	99.22	99.35	100.14
Mg no.	51	58	58	55	67	69	66	57	57	60	59	58	58	59	39	47	58
Na_2O+K_2O	7.89	6.40	6.43	6.91	5.88	5.47	5.53	6.17	5.16	6.12	5.82	7.07	7.17	6.97	7.83	7.98	8.28
La	29.97	45.80	44.53	40.10	15.41	20.97	14.03	36.09	31.42	33.54	33.68	30.05	29.13	29.44	27.02	47.92	28.09
Ce	61.04	88.29	85.99	78.44	32.40	45.52	27.73	69.10	61.92	63.04	64.69	55.56	54.95	55.36	58.16	82.82	57.54
Pr	7.72	10.21	10.11	9.35	3.77	5.37	3.27	8.02	7.31	7.42	7.58	6.42	6.22	6.23	7.00	9.00	6.71
Nd	30.96	37.28	36.31	34.85	15.41	22.08	12.48	29.02	26.53	27.72	27.76	23.26	22.92	22.85	29.37	31.56	27.01
Sm	5.39	6.39	6.38	6.05	3.22	4.54	2.52	4.67	4.57	4.56	4.60	4.22	4.10	4.17	5.31	5.03	5.11
Eu	1.54	1.64	1.56	1.58	0.88	1.32	0.69	1.36	1.16	1.37	1.30	1.21	1.22	1.19	1.78	1.04	1.59
Gd	4.27	5.14	5.04	4.82	2.65	3.57	2.37	3.90	3.81	3.71	3.81	3.46	3.55	3.47	4.16	3.62	4.06
Tb	0.56	0.70	0.66	0.64	0.40	0.55	0.33	0.51	0.50	0.47	0.49	0.46	0.48	0.47	0.58	0.47	0.61
Dy	3.06	3.55	3.51	3.37	2.01	2.84	1.86	2.82	2.71	2.53	2.69	2.59	2.55	2.54	2.92	2.37	3.27
Ho	0.58	0.65	0.64	0.62	0.40	0.57	0.36	0.55	0.52	0.49	0.52	0.49	0.49	0.49	0.59	0.42	0.62
Er	1.61	1.74	1.69	1.68	1.00	1.41	0.82	1.44	1.33	1.30	1.35	1.34	1.35	1.35	1.56	1.09	1.49
Tm	0.23	0.24	0.22	0.23	0.15	0.22	0.13	0.20	0.17	0.18	0.18	0.19	0.19	0.18	0.26	0.17	0.23
Yb	1.50	1.54	1.45	1.50	0.94	1.35	0.74	1.30	1.14	1.15	1.20	1.20	1.26	1.22	1.57	1.07	1.39
Lu	0.23	0.23	0.22	0.23	0.15	0.20	0.09	0.19	0.16	0.17	0.18	0.18	0.19	0.18	0.26	0.17	0.21
REE	148.68	203.41	198.31	183.47	78.79	110.52	67.42	159.17	143.26	147.65	150.03	130.63	128.62	129.15	140.52	186.75	137.91
$(La/Yb)_N$	3.96	3.84	3.67	3.71	4.74	3.58	3.15	3.70	3.23	3.49	3.47	3.38	3.23	3.23	3.81	3.72	3.15
Eu/Eu*	0.96	0.86	0.82	0.88	0.90	0.97	0.86	0.95	0.84	1.00	0.93	0.95	0.97	0.94	1.13	0.72	1.04
V	150.15	90.80	82.79	107.91	*nd*	*nd*	*nd*	105.81	108.25	103.12	105.73	108.30	117.66	117.60	*nd*	*nd*	*nd*
Cr	15.02	118.74	113.41	82.39	*nd*	*nd*	*nd*	302.21	320.96	295.27	306.15	169.82	179.77	177.32	*nd*	*nd*	*nd*
Co	20.79	17.63	16.90	18.44	*nd*	*nd*	*nd*	26.17	28.93	26.11	27.07	17.01	17.59	18.47	*nd*	*nd*	*nd*
Ni	22.18	76.72	97.49	65.46	*nd*	*nd*	*nd*	189.85	263.68	226.43	226.66	63.93	71.88	65.89	*nd*	*nd*	*nd*
Rb	137.98	58.57	54.36	83.63	53.90	51.74	45.24	51.11	75.38	55.18	60.56	83.99	87.20	89.97	151.67	112.96	392.45
Sr	444.29	640.04	476.01	520.11	623.78	645.74	550.19	1198.54	1002.96	1137.99	1113.16	616.36	654.66	568.89	313.31	410.91	679.84
Y	15.03	17.25	16.81	16.36	100.42	14.12	9.93	14.12	14.57	13.04	13.91	12.99	13.25	12.96	15.06	11.45	15.58
Zr	161.32	261.51	248.72	223.85	115.19	140.52	105.88	164.08	163.46	162.12	163.22	139.57	135.08	126.81	151.36	214.33	158.36
Nb	7.88	12.42	12.66	10.99	4.33	4.61	4.08	10.16	10.14	10.02	10.11	9.27	9.39	9.51	7.39	13.42	9.28
Ba	565.43	1059.66	1006.00	877.03	637.75	532.88	399.88	982.32	722.62	983.99	896.31	1179.01	1245.23	1120.86	2126.81	1042.57	1060.36
Ta	0.53	0.92	0.96	0.80	0.36	0.34	0.29	0.68	0.65	0.65	0.66	0.65	0.63	0.64	0.42	1.11	0.59
Pb	7.00	27.84	21.24	18.69	18.69	15.03	28.11	15.03	15.43	14.97	15.14	15.07	14.95	25.15	4.83	18.96	5.10
Th	4.33	16.65	16.85	12.61	6.73	6.39	4.22	6.35	6.01	5.80	6.05	8.33	8.12	7.91	3.84	29.37	4.91
U	1.56	3.91	4.15	3.21	2.18	1.70	1.37	1.47	1.39	1.29	1.38	1.81	1.81	1.75	0.93	3.85	1.35
Hf	3.97	6.49	6.15	5.54	2.91	3.25	2.03	4.09	3.93	3.75	3.92	3.76	3.71	3.34	3.60	3.57	3.76

*Data from Chen *et al*. (2005); nd – not detected; Mg no. = 100 × Mg/(Mg + $\sum$Fe) in atomic ratio; LOI – loss on ignition.

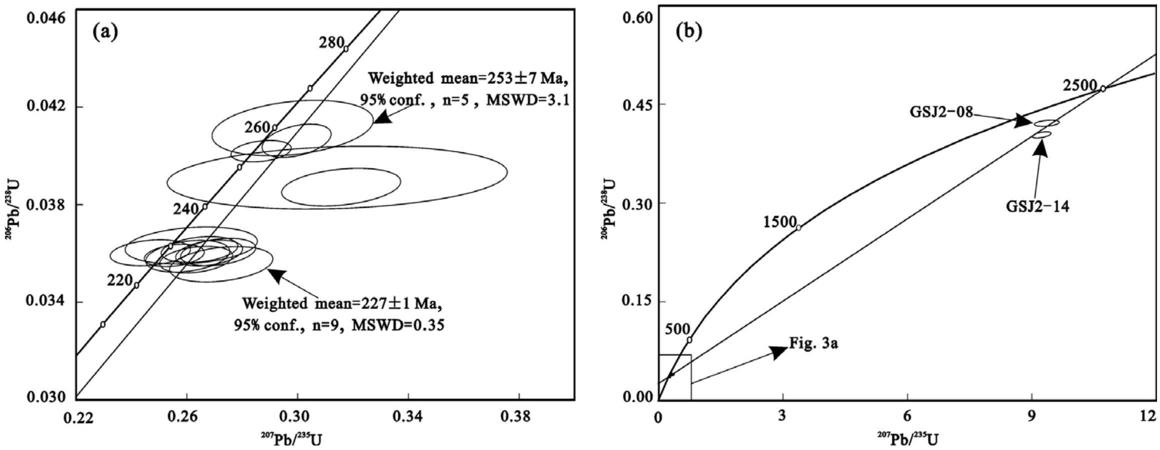

Figure 3. U–Pb concordia diagrams for zircons of GSJ2 from Jinchanggouliang (JCGL). Conf. – confidence; MSWD – mean square of the weighted deviates.

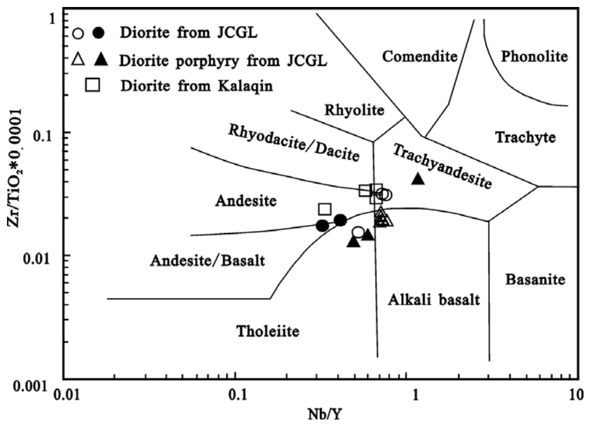

Figure 4. Nb/Y–Zr/TiO_2*0.001 diagram for dykes from Jinchanggouliang (JCGL) (modified from Winchester & Floyd, 1977). Data for the diorite and diorite porphyry from JCGL illustrated by hollow circles and triangles are from this study. Data shown by solid circles and triangles are from Chen *et al.* (2005). Kalaqin diorites (hollow squares) are from Han, Shao & Zhou (2000).

6. Discussion

6.a. Petrogenesis of the JCGL dykes

6.a.1. Crustal contamination

Previous investigations generally agree that the magmas emplaced in the interior of a continent experience some degree of crustal contamination during ascent and/or residence within crustal magma chambers (e.g. Currie & Williams, 1993). Models invoking crustal assimilation may account for some trace element and isotopic variations observed in Figures 6–9. However, crustal assimilation cannot explain the high concentrations of Ba (399.88–2126.81 ppm) and Sr (313.31–1198.54 ppm) in the JCGL dykes (Table 2), which are much higher than continental crust values (Ba = 259–550 ppm, Sr = 281–350 ppm; Rudnick & Fountain, 1995). Moreover, random or no correlations have been observed in the diagram of $(^{87}Sr/^{86}Sr)_i$ versus MgO and SiO_2 (Fig. 10), which precludes the possibility of extensive crustal contamination. Hence, the magmatic evolution of the JCGL dykes is not significantly affected by crustal contamination, and the geochemical and isotopic signatures of these dykes were mainly inherited from their magma sources.

6.a.2. Magma source

The inherited or captured Archaean zircons and whole-rock geochemistry characteristics (such as positive Pb anomaly) all indicate that a crustal component was involved in the magma source of these dykes. Han, Shao & Zhou (2000) contended that the Kalaqin diorite, which has a similar emplacement time and geochemical characteristics to the JCGL dykes (Figs 1, 4, 6, 7), was derived from partial melting of the lower crust of the NCC. However, experimental data have shown that regardless of the degree of partial melting, melts from metabasalts of the lower crust are generally characterized by low Mg numbers (<45; Rapp & Watson, 1995), which is not the case for the JCGL dykes (39–69, mostly >50). Therefore, these dykes cannot be generated by remelting of the basic lower crustal rocks only, but a mantle source is required. This conclusion is supported by the relatively high contents of Cr (320.96 ppm) and Ni (263.68 ppm) of some samples and occurrences of contemporary cumulate xenoliths in the Kalaqin region (Shao *et al.* 1999).

The question remains whether these mantle-derived magmas originated from the lithospheric mantle or the asthenosphere. The Sr, Nd and Pb isotope data of the JCGL dykes provide further information on the nature of their source region. As mentioned above, the NCC is an Archaean craton. However, the lithospheric mantle beneath it was formed in the Archaean and replaced in the Proterozoic beneath the central portion of the craton, based on the Re depletion ages of 2.6–3.2 Ga for peridotite xenoliths in the Palaeozoic diamondiferous kimberlites from Mengyin and Fuxian (Gao *et al.* 2002; Wu *et al.* 2006; Zhang *et al.* 2008*a*), and that of 1.9 Ga for peridotite xenoliths in the Neogene alkali

https://doi.org/10.1017/S0016756811000173 Published online by Cambridge University Press

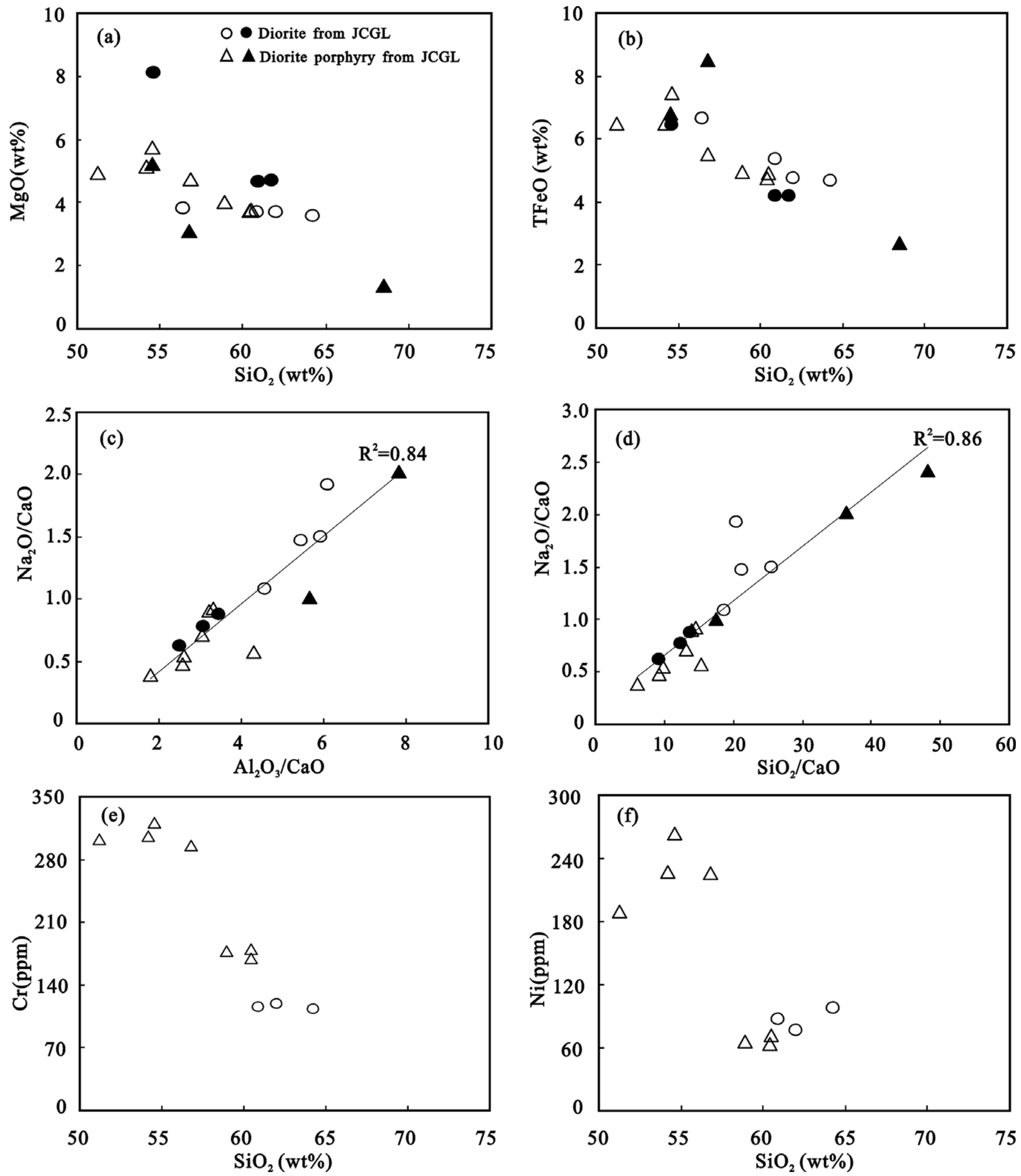

Figure 5. Variation of (a) MgO versus SiO_2, (b) TFeO versus SiO_2, (c) Na_2O/CaO versus Al_2O_3/CaO, (d) Na_2O/CaO versus SiO_2/CaO, (e) Cr versus SiO_2 and (f) Ni versus SiO_2. The grey lines in (c) and (d) indicate regression analysis of rocks with associated R^2 value. Data source is the same as Figure 4.

basalts from Hannuoba (Gao *et al.* 2002). Assuming that the Palaeozoic lithospheric mantle of the NCC originated from evolutional Proterozoic lithospheric mantle, Han, Kagami & Li (2004) calculated that the lowest ε_{Nd} (220 Ma) was about −8.8, which was nearly the same as the ε_{Nd} (135 Ma) value of −8.2 from EM1-affinity lithospheric mantle beneath the Taihangshan region (Chen, Jahn & Zhai, 2003; Chen & Zhai, 2003). These isotope values are also consistent with the Fanshan potassic alkaline ultramafite–syenite complex (ε_{Nd} (240 Ma) = −5.8; Mu *et al.* 2001) and Datong lamprophyre (Fig. 8; ε_{Nd} (220 Ma) = −5.4; Shao *et al.* 2003) from the northern margin of the NCC, which are all regarded to have resulted from partial melting of the lithospheric mantle (Figs 1b, 11c). The participation of enriched lithospheric mantle can reasonably account for the source properties of some JCGL dykes with high Ba and Sr contents, $\varepsilon_{Nd}(t)$ values of −8.9 to −12, T_{DM2} ages of 1721–1972 Ma (Table 3; Fig. 8b) and the wide range of Pb isotope compositions (Fig. 9). A simple mass balance calculation based on the Sr and Nd isotopes shows that the mixing of less than 13 % lower crustal melts with the magma derived from EM1-like lithospheric mantle can produce the observed

https://doi.org/10.1017/S0016756811000173 Published online by Cambridge University Press

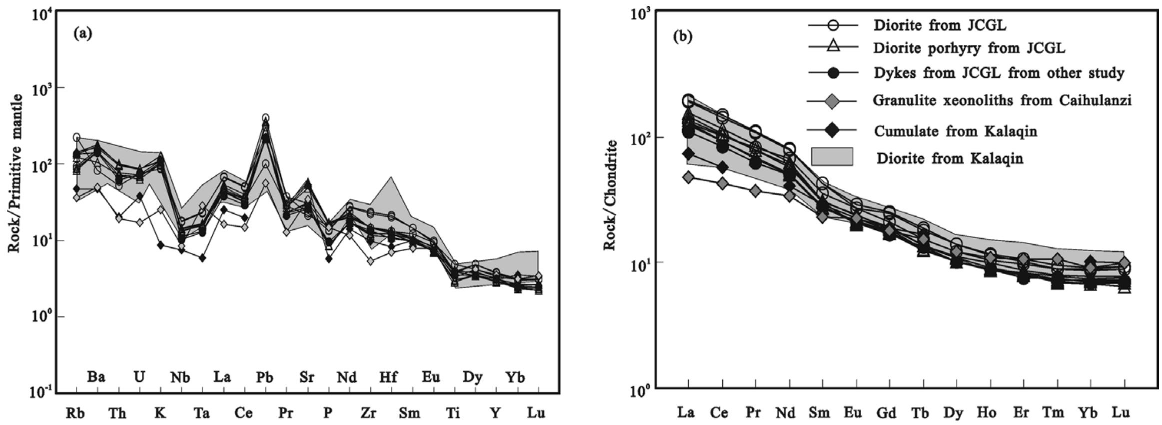

Figure 6. (a) Primitive mantle-normalized trace element distributions and (b) chondrite-normalized REE patterns. The primitive mantle and chondrite values are from Sun & McDonough (1989). Data for dykes from Jinchanggouliang (JCGL) from other study are from Chen *et al.* (2005) (average value of six samples); data for granulite xenoliths in Caihulanzi are from She *et al.* (2006); cumulate in Kalaqin from Shao *et al.* (1999) (average value of 22 samples); and for diorite in Kalaqin from Han, Shao & Zhou (2000).

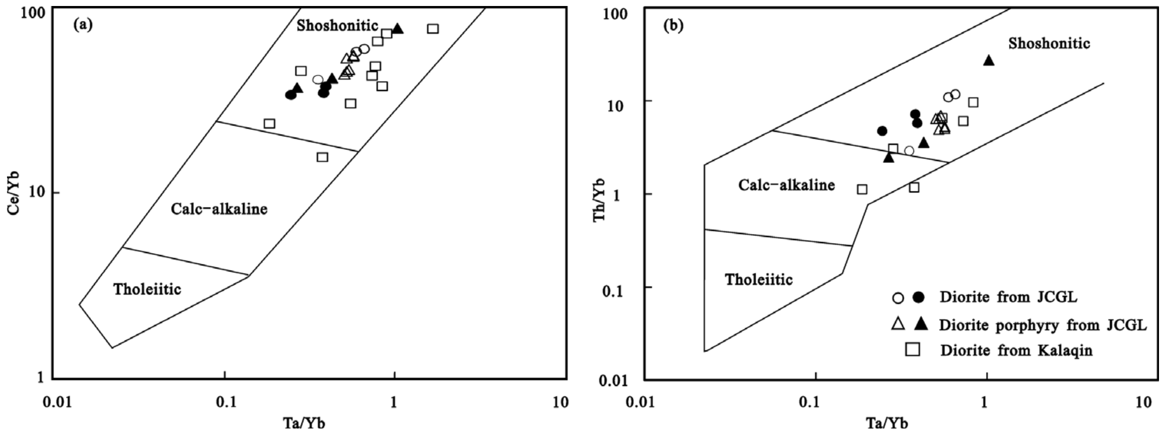

Figure 7. (a) Ta/Yb–Ce/Yb and (b) Ta/Yb–Th/Yb diagrams for dykes from JCGL (modified from Pearce, 1982). Data source is the same as Figure 4.

Sr/Nd isotopic ratios of these dykes (curve B in Fig. 8a).

However, mixing of the lower crust and enriched lithospheric mantle cannot perfectly explain the higher $\varepsilon_{Nd}(t)$ (1.1 to −3.7) and younger T_{DM2} ages (913–1300 Ma) of other samples (Table 3; Fig. 8), because the NCC sub-continental lithospheric mantle was enriched and had not undergone significant crustal growth after the Proterozoic. In contrast, these Sr–Nd isotopic characteristics are similar to the Phanerozoic igneous rocks from the CAOB (Fig. 8; Wu *et al.* 2000; Hong *et al.* 2000; Zhou *et al.* 2001, 2009; Zhang *et al.* 2008*b*). Their geochemical features could be related to the injection of ascending asthenospheric mantle melt following detachment of the subducting slab from the Palaeo-Asian Ocean and magma underplating, or the injection of melt and fluid from the subducted slab itself. However, no early Mesozoic adakite or high magnesium andesite, products of melting hot and young oceanic crust, have been found in the adjacent areas. Hence, we speculate that the magma source of these dykes with higher $\varepsilon_{Nd}(t)$ and younger T_{DM2} ages may be related to the ascending asthenospheric mantle melt. Furthermore, exposure of the contemporaneous cumulate (220–237 Ma; Shao *et al.* 1999, 2000) and granulite xenoliths (220–251 Ma; Shao, Han & Li, 2000; She *et al.* 2006) in Kalaqin and Caihulanzi (Figs 1b, 11c) imply that a process of asthenospheric magma underplating and the formation of juvenile lithospheric mantle played a role in the magma genesis. The most recent investigations for the Faku gabbro also demonstrate the presence of juvenile lithospheric mantle with an affinity of the CAOB beneath the NCC in northern Liaoning Province during early Mesozoic time (Fig. 11c; Zhang *et al.* 2009*a*). High $\varepsilon_{Hf}(t)$ values (−2.9 to 1.7) and young Hf isotopic model ages (T_{DM} = 0.81−0.98 Ga) of the Xiaozhangjiakou mafic–ultramafic (XZJK) complex also provide direct evidence for the existence of asthenospheric melt in the magma source region (Figs 1b, 11c; Tian *et al.* 2007). Consequently, this melt may have been generated from the underplated asthenospheric melt following the detachment of a subducting slab (Zhang *et al.* 2009*b*).

Overall, the JCGL dykes originated from mixing of the lower crust, lithospheric mantle of the NCC and ascending asthenospheric mantle melt following detachment of a subducting slab and magma underplating (Fig. 11).

https://doi.org/10.1017/S0016756811000173 Published online by Cambridge University Press

Table 3. Sr–Nd–Pb isotope compositions of dykes from the JCGL

Rock type	diorite						diorite porphyry								
Sample No.	SCJ1	SCJ3	SCJ4	J26–211-1*	J13–1*	Jc91–11-2*	SCJ6	SCJ7	SCJ8	SCB1	SCB2	SCB3	J26–13-5–2*	Jc91–4*	J26–711-1–3*
Rb (ppm)	137.20	57.71	54.57	48.21	42.34	47.26	50.96	75.10	54.99	84.54	88.73	88.66	154.10	408.60	108.00
Sr (ppm)	465.10	669.90	499.80	673.30	657.10	656.90	1416.00	1033.00	1234.00	664.00	705.10	601.50	321.40	720.60	427.80
$^{87}Rb/^{86}Sr$	0.8503	0.2483	0.3148	0.2053	0.1844	0.2059	0.1038	0.2097	0.1285	0.3670	0.3628	0.4249	1.3755	1.6252	0.7235
$^{87}Sr/^{86}Sr$	0.707700	0.706540	0.706780	0.705592	0.705977	0.705385	0.706260	0.706050	0.706290	0.706540	0.706670	0.706410	0.708603	0.709205	0.708012
2σ	10	50	50	13	12	13	60	40	50	60	50	10	12	13	13
$(^{87}Sr/^{86}Sr)_i$	0.70495	0.70574	0.70576	0.70493	0.70538	0.70472	0.70592	0.70537	0.70587	0.70535	0.70549	0.70503	0.70415	0.70394	0.70567
Sm (ppm)	5.29	6.29	6.14	3.58	4.12	4.95	4.44	4.37	4.46	4.03	4.08	3.97	5.65	5.98	5.03
Nd (ppm)	29.51	37.44	35.33	17.42	19.93	25.92	27.72	25.86	26.68	22.58	22.57	21.93	30.26	31.37	31.96
$^{147}Sm/^{144}Nd$	0.1084	0.1017	0.1052	0.1243	0.1251	0.1157	0.0969	0.1022	0.1011	0.1078	0.1094	0.1096	0.1130	0.1155	0.0953
$^{143}Nd/^{144}Nd$	0.511893	0.512483	0.512491	0.512586	0.512557	0.512493	0.512035	0.512012	0.512026	0.512318	0.512319	0.512331	0.512012	0.512193	0.512302
1σ	9	3	2	12	11	9	3	6	3	6	2	3	11	11	11
$\varepsilon_{Nd}(t)$	−12.0	−0.3	−0.2	1.1	0.5	−0.5	−8.9	−9.5	−9.2	−3.7	−3.7	−3.5	−9.8	−6.3	−3.6
T_{DM2} (Ma)	1972	1023	1019	913	961	1040	1721	1770	1745	1299	1301	1283	1795	1515	1295
$^{206}Pb/^{204}Pb$	17.999	17.481	17.337	nd	nd	nd	16.725	16.646	16.668	17.845	17.731	17.592	nd	nd	nd
$^{207}Pb/^{204}Pb$	15.548	15.378	15.342	nd	nd	nd	15.286	15.242	15.226	15.573	15.429	15.511	nd	nd	nd
$^{208}Pb/^{204}Pb$	38.177	37.574	37.417	nd	nd	nd	36.952	36.723	36.693	38.317	37.85	37.951	nd	nd	nd
$(^{206}Pb/^{204}Pb)_i$	17.436	17.331	17.149	nd	nd	nd	16.495	16.454	16.434	17.640	17.522	17.471	nd	nd	nd
$(^{207}Pb/^{204}Pb)_i$	15.520	15.371	15.333	nd	nd	nd	15.275	15.232	15.214	15.563	15.419	15.505	nd	nd	nd
$(^{208}Pb/^{204}Pb)_i$	37.676	37.090	36.775	nd	nd	nd	36.610	36.408	36.379	37.870	37.412	37.696	nd	nd	nd

*Data from Chen *et al.* (2008); nd – not detected; $(^{87}Sr/^{86}Sr)_i$ and $\varepsilon_{Nd}(t)$ values are calculated at $t = 227$ Ma based on present-day $(^{147}Sm/^{144}Nd)_{CHUR} = 0.1967$ and $(^{143}Nd/^{144}Nd)_{CHUR} = 0.512638$. T_{DM2} values are calculated based on present-day $(^{147}Sm/^{144}Nd)_{DM} = 0.2137$ and $(^{143}Nd/^{144}Nd)_{DM} = 0.51315$. $\lambda_{Rb} = 1.42 \times 10^{-11}$ year^{-1} (Steiger & Jäger, 1977), $\lambda_{Sm} = 6.54 \times 10^{-12}$ year^{-1} (Lugmair & Harti, 1978).

6.b. Geodynamic significance

6.b.1. Implications for evolution of the CAOB

As described in the introduction, the timing of the final closure of the Palaeo-Asian Ocean has long been controversial. Some authors propose that the suturing took place during Late Permian to Early Triassic time (Chen *et al.* 2000; Davis *et al.* 2001; Xiao *et al.* 2003); whereas others prefer suturing during either Middle Devonian time (Tang, 1990; Xu & Chen, 1997) or Late Devonian–Early Carboniferous time (Shao, 1991; Hong *et al.* 1995). In combination with investigations of palaeontology and palaeoclimate, the new geochronology data from retrograded eclogites, ophiolites and multiple mafic to acid igneous rocks from the northern margin of the NCC and CAOB provide important constraints on this issue.

The retrograded eclogites, which have tholeiitic protoliths (mid-ocean ridge basalt or island arc tholeiite) and eclogite facies metamorphism, exist in the Zhangjiakou region (Fig. 1b). Zircon SHRIMP isotopic dating of these rocks defines a weighted mean age of ~ 325 Ma, which was interpreted as the peak metamorphic age and reflects the subduction of Palaeo-Asian oceanic lithosphere beneath the NCC (Ni *et al.* 2006). Recently, a late Palaeozoic continental arc magmatic belt (calc-alkaline or high-K calc-alkaline gabbroic to granitic rocks) was identified on the northern margin of the NCC, which was thought to have been related to S-dipping subduction of the Palaeo-Asian oceanic slab beneath the NCC, and it existed for about 50 Ma (320–270 Ma; Zhang *et al.* 2007, 2009*c*; Chen, Jahn & Tian, 2009; Jian *et al.* 2010). Radiolarians found in the argillite beds of the Zhesi Formation from the Zhesi and Xilinhot areas (Fig. 1a) also indicate that a deep marine sedimentary facies persisted during Middle Permian time and the Palaeo-Asian Ocean was not closed until this time (Shang, 2004). Moreover, the youngest ENE-trending ophiolite belts found in the CAOB are Late Permian in age, such as the Solon Obo (279 Ma), Ondor Sum (260 Ma) and Banlashan (256 Ma) (Miao *et al.* 2007), and the undeformed granodioritic dykes intruded the Hegenshan ophiolite (with a zircon U–Pb age of 298 ± 9 Ma) at 244 ± 4 Ma (Miao *et al.* 2008). Based on these observations, we speculate that the final closure of the Palaeo-Asian Ocean and collision between the southern Mongolian terranes and NCC probably took place in latest Permian to earliest Triassic time (*c.* 250 Ma; Fig. 11a). This conclusion is also supported by the palaeoclimatic evidence. Cope *et al.* (2005) noted that a widespread climate change took place in North China, which is recorded by a change from the Carboniferous–Early Permian humid climate with coal-bearing sedimentary facies to a Late Permian–Early Triassic arid climate with redbeds.

Liégeois (1998) divided an orogenic cycle into four stages: a pre-collisional period characterized by subduction, an arc-continent or continent–continent collision period accommodated by crustal thickening,

Table 4. Isotope data used for the mixing calculation

	Sr (ppm)	Nd (ppm)	$^{87}Sr/^{86}Sr$	$\varepsilon_{Nd}(t)$	Source
Xilinhot basalt	181	13	0.704	7	Zhang *et al.* 2008*b*
EM1	1100	30	0.705	−8.2	Chen, Jahn & Zhai, 2003; Chen & Zhai, 2003
DM	20	1.2	0.703	8	Wu *et al.* 2003
LCC	300	24	0.710	−30	Jahn *et al.* 1999
UCC	350	26	0.720	−10	Jahn *et al.* 1999

EM1 – enriched mantle 1; DM – depleted mantle; LCC – lower continental crust; UCC – upper continental crust.

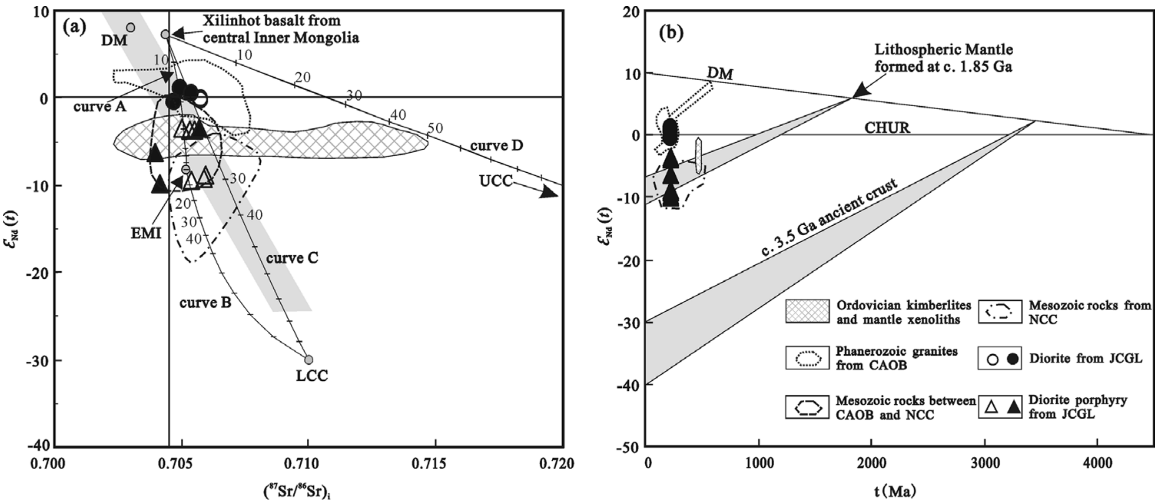

Figure 8. (a) $\varepsilon_{Nd}(t)$ versus $(^{87}Sr/^{86}Sr)_i$ showing mixing proportions between two end members. The end-member data used for the binary mixing calculation are listed in Table 4. Curves A, B, C and D refer to the mixing between EM1-like sub-continental lithospheric mantle (SCLM) and the Xilinhot basalt from central Inner Mongolia, which represents basaltic melts from the asthenosphere of the Central Asian Orogenic Belt (CAOB); EM1-type SCLM and the lower crust; Xilinhot basalt and the lower crust; and Xilinhot basalt and the upper crust, respectively. The tick marks and numbers denote the proportions of lower continental crust (LCC) or enriched mantle 1 (EM1) in 10 % increments. (b) $\varepsilon_{Nd}(t)$ versus crystallization age plots for rocks from Jinchanggouliang (JCGL). The ancient crust evolution line is constructed on the basis of an average $^{147}Sm/^{144}Nd$ value of 0.118 (Jahn & Condie, 1995). The lithospheric mantle evolution line is from Han, Kagami & Li (2004). Ordovician kimberlites and mantle xenoliths in the eastern North China craton (NCC) are from Zheng & Lu (1999), Wu *et al.* (2006) and Zhang & Yang (2007). Phanerozoic granites in the CAOB are from Wu *et al.* (2000), Hong *et al.* (2000), Zhou *et al.* (2001, 2009) and Zhang *et al.* (2008*b*). Isotope compositions of Mesozoic volcanic rocks from the transitional part of the CAOB and NCC are from Zhou *et al.* (2001). Mesozoic rocks from the NCC include Triassic alkaline intrusives in the Yanliao–Yinshan area (Yan *et al.* 1999), the Fanshan potassic alkaline ultramafite–syenite complex (Mu *et al.* 2001), Datong lamprophyre (Shao *et al.* 2003), Guangtoushan alkaline granite (Han, Kagami & Li, 2004) and late Mesozoic basalt from the northern margin of the NCC (Zhang *et al.* 2004). Data for diorite and diorite porphyry from JCGL (solid circles and triangles) are from Chen *et al.* (2008). All data is calculated at 230 Ma.

a post-collisional period and a post-orogenic period. Following this context and the regional magmatism mentioned above, the northern margin of the newly amalgamated North China–Mongolian plate was dominated by post-orogenic regimes during Triassic time (250–200 Ma; Fig. 11b). The prevailing orientations of dyke strikes, as illustrated in the rose diagram in Figure 1c, are nearly the same as those of the maximum principal compressive stress in the NCC during latest Permian to earliest Triassic time (160°–178°; Wan, 2004; Hou, Wang & Hari, 2010), which is also orthogonal to the collisional belt between the NCC and Mongolian arc terranes (Fig. 1a). This phenomenon indicates that dykes were intruded into tensional faults or fractures that formed synchronously with compression during the period of collision between the southern Mongolian terranes and the NCC. Though the faults hosting the shoshonitic dykes formed in a compressional environment, the asthenospheric mantle source of the dykes may also reflect a tensional environment, parallel to the orogene, when the dykes intruded. Away from mid-ocean ridges and hot spots, magma from the asthenosphere is unable to reach the surface because the asthenosphere is deeper, heat flow is lower and the material is confined under higher pressure by a greater thickness of the overlying lithosphere. No evidence for mid-ocean ridges or hot spots exists on the northern margin of the NCC during Triassic time. Therefore, the asthenospheric mantle-derived melt generation in the JCGL must reflect some additional process that resulted in the upwelling of asthenospheric mantle in the Triassic. This may be associated with the lithosphere extension resulting from post-orogenic subduction slab detachment or lithospheric delamination (Fig. 11b). Although these shoshonitic dykes may also have formed in strike-slip or transtensional tectonic regimes (Vaughan, 1996), the ENE-trending Datong lamprophyre belt (Fig. 1b;

https://doi.org/10.1017/S0016756811000173 Published online by Cambridge University Press

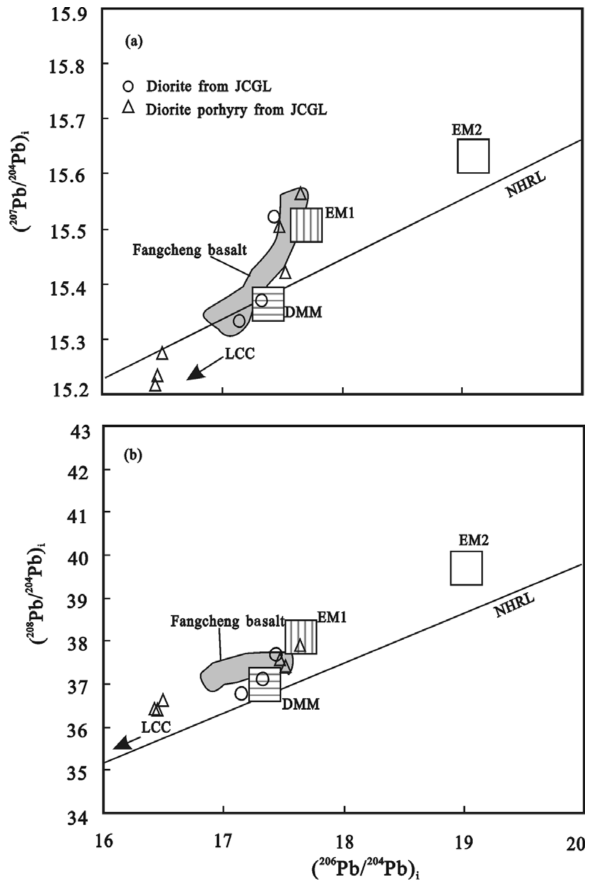

Figure 9. (a) Plot of $(^{207}Pb/^{204}Pb)_i$ versus $(^{206}Pb/^{204}Pb)_i$ and (b) Plot of $(^{208}Pb/^{204}Pb)_i$ versus $(^{206}Pb/^{204}Pb)_i$ for dykes from JCGL. NHRL – Northern Hemisphere reference line. Locations of EM1, EM2 and DMM (depleted MORB mantle) are from Zindler & Hart (1986). Late Mesozoic Fangcheng basalts (Zhang *et al*. 2002) were plotted for reference. Data source is the same as Figure 8.

220 Ma; Shao *et al*. 2003), the Triassic A-type granite belt (Fig. 1b; 220–240 Ma, including alkali granite in Guangtoushan and a syenogranite dyke and monzogranite in Jianping; Han, Kagami & Li, 2004; Zhang *et al*. 2009*c*) and the alkaline intrusions belt (Yan *et al*. 1999; Mu *et al*. 2001) from the continental interior of the NCC, are all orthogonal to the extension direction implied by the subduction zone (Figs 1, 11) and preclude these possibilities. The exposure of a Late Triassic metamorphic core complex in the Solonker suture belt also indicates the dominance of extensional tectonics (Davis *et al*. 2004).

Combined with the observations mentioned above, we argue that a post-orogenic extensional regime, resulting from the post-collisional subduction slab detachment or lithospheric delamination and magma upwelling, explains the geodynamic setting of these dykes. There are several other lines of evidence supporting magma upwelling and continental crustal growth during Triassic time. The exposure of contemporaneous cumulate (220–237 Ma; Shao *et al*. 1999, 2000) and granulite xenoliths (220–251 Ma; Shao, Han & Li, 2000; She *et al*. 2006) in Kalaqin and Caihulanzi (Figs 1b, 11c) imply that the process of asthenospheric magma underplating and the formation of juvenile lithospheric mantle played a key role in the dykes genesis. The geochemical features of the Middle Triassic mafic–ultramafic complex from Xiaozhangjiakou (XZJK), high $\varepsilon_{Hf}(t)$ values (−2.9 to 1.7) and young Hf isotopic model ages (T_{DM} = 0.81−0.98 Ga), also provide direct evidence for the asthenospheric magma underplating (Figs 1b, 11c; Tian *et al*. 2007).

Consequently, the regional magmatism reflects an integrated orogenic cycle from the collision between the southern Mongolian arc terranes and the NCC to post-orogenic periods. The final collision of these two blocks occurred in Late Permian to Early Triassic time and was immediately followed by the post-collisional/post-orogenic extension geodynamic regimes during Triassic time, in which the JCGL shoshonitic dykes intruded.

6.b.2. Implications for modification of the mantle beneath the NCC in the early Mesozoic

Studies of the late Mesozoic basalts and lamprophyres suggest the existence of an EM1-like SCLM beneath the NCC (e.g. Zhang *et al*. 2002; Chen, Jahn &

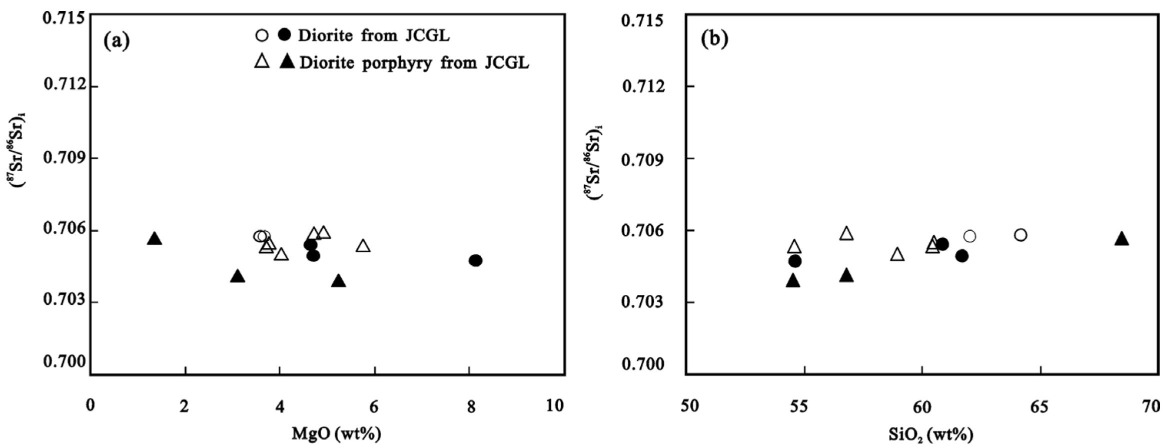

Figure 10. (a) $(^{87}Sr/^{86}Sr)_i$ versus MgO (wt %) and (b) $(^{87}Sr/^{86}Sr)_i$ versus SiO_2 (wt %) diagrams for dykes from JCGL showing there is no obvious correlation. Data source is the same as Figure 8.

https://doi.org/10.1017/S0016756811000173 Published online by Cambridge University Press

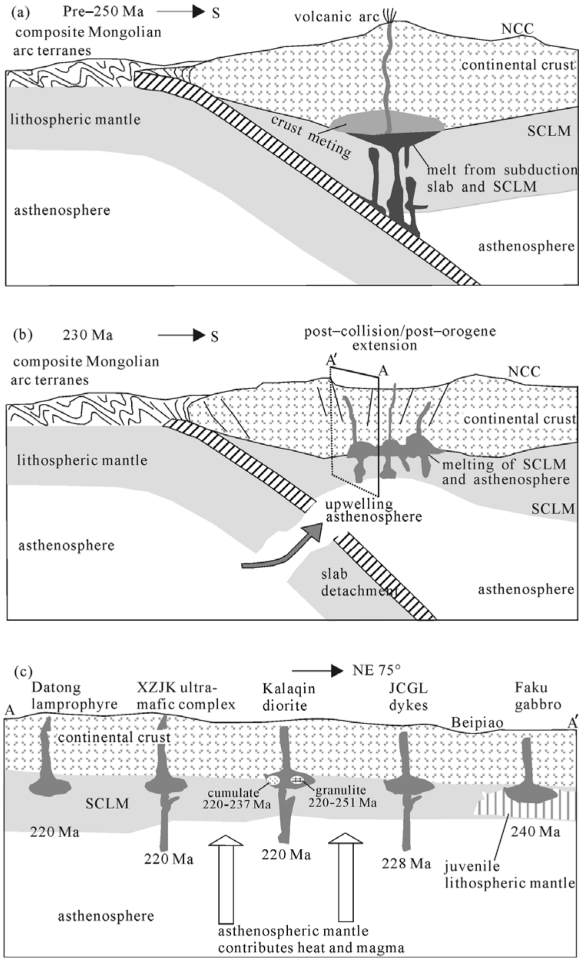

Figure 11. Tectonomagmatic model for the Jinchanggouliang (JCGL) shoshonitic dykes and mafic–ultramafic rocks from adjacent areas. (a) Pre-250 Ma: the North China craton (NCC) and the southern Mongolian terranes were amalgamated and behaved as a combined North China–Mongolian plate (modified from Zhang *et al.* 2009*c*). (b) 230 Ma: combined North China–Mongolian plate entered into the post-collisional/post-orogenic extensional environment (modified from Zhang *et al.* 2009*c*; Pe-Piper *et al.* 2009). Location of A–A′ cross-section plane shown. (c) Magma source of the JCGL dykes and mafic–ultramafic rocks from adjacent areas of the A–A′ cross-section plane (for discussion and data source, see text). Schematic location of the A–A′ section plane is shown in Figure 1. Illustrations are not to scale.

Zhai, 2003; Chen & Zhai, 2003). However, owing to the intensive thinning and replacement of lithospheric mantle in late Mesozoic time (e.g. Zhang *et al.* 2002; Rudnick *et al.* 2004), little is known about the composition and process of the SCLM beneath the NCC in late Palaeozoic to early Mesozoic time. Additionally, the initiation time for lithospheric thinning is still controversial (Wu *et al.* 2008; Xu *et al.* 2009). Although most researchers believe that the destruction of the NCC occurred during late Mesozoic time (e.g. Zhang *et al.* 2002; Menzies *et al.* 2007), other researchers proposed that the destruction probably began in early Mesozoic time (e.g. Han, Kagami & Li, 2004). In a recent paper by Zhang *et al.* (2009*b*), it is proposed that the lithospheric destruction and thinning of the northern NCC began in Middle–Late Triassic time.

The newly recognized intermediate-mafic shoshonitic dykes provide new constraints on the isotopic compositions and evolution of the mantle reservoirs beneath the northern NCC. Low initial $(^{87}Sr/^{86}Sr)_i$ ratios, significantly negative $\varepsilon_{Nd}(t)$ values and enrichment in LILE (e.g. Sr and Ba) of the JCGL dykes imply that slightly enriched lithospheric mantle still existed in Late Triassic time. Nevertheless, this enriched SCLM had been modified, weakened and had become thermally and mechanically unstable as indicated by the involvement of underplated asthenospheric melt in the source of the JCGL dykes. Involvement of the underplating asthenospheric melt in magmatism has been considered as an important signal for lithospheric destruction, reactivation or craton thinning (e.g. Zhang *et al.* 2009*b*; Xu *et al.* 2009). The mixed sources of the JCGL dykes (lower crust, SCLM and asthenospheric melt) suggests that the onset of lithospheric destruction and thinning in the northern NCC occurred in Middle–Late Triassic time as a result of post-collisional/post-orogenic subduction slab detachment or lithospheric delamination as suggested by Zhang *et al.* (2009*b*; Fig. 11).

7. Conclusions

(1) The JCGL dykes intruded at 227 Ma. They are enriched in LILE and LREE without significant Eu anomalies, depleted in HFSE and show some features of shoshonitic rocks.

(2) Low initial $^{87}Sr/^{86}Sr$ ratios (0.70394 to 0.70592), and a wide range of $\varepsilon_{Nd}(t)$ (1.1 to −12.0) and Pb isotope compositions suggest that these dykes might have originated from mixing of the lower crust, lithospheric mantle of the NCC and asthenospheric melt.

(3) These post-orogenic shoshonitic dykes indicate that closure of Palaeo-Asian Ocean had completed before Middle Triassic time, and the CAOB was subsequently tectonically dominated by post-orogenic regimes. Correspondingly, thinning and replacement of the lithospheric mantle beneath the NCC started from Middle Triassic time at least on the northern margin.

Acknowledgements. We thank Y. S. Liu, H. F. Tang, Y. F. Ge and F. X. Cao for their thoughtful comments. S. Zheng and H. H. Chen are acknowledged for their help during LA-ICP-MS U–Pb dating. We are also grateful to two anonymous reviewers for their constructive suggestions, and Dr M. Allen, Taylor Bowen and Kat Piper for their editorial handling. This research was financially supported by the Chang Jiang Scholars and Innovation Group Programme, the Crisis Mines Substitute Resources Prospecting Project, China (Grant No. 2006020035), the Natural National Science Foundation, China (91014002), the academic exploration fund for graduates from China University of Geosciences (CUGYJS0812), and the State Key Laboratory of Geological Processes and Mineral Resources, China University of Geosciences.

https://doi.org/10.1017/S0016756811000173 Published online by Cambridge University Press

References

ADAMS, M. G., LENTZ, D. R., SHAW, C. S. J., WILLIAMS, P. F., ARCHIBALD, D. A. & COUSENS, B. 2005. Eocene shoshonitic mafic dykes intruding the Monashee Complex, British Columbia: a petrogenetic relationship with the Kamloops Group volcanic sequence. *Canadian Journal of Earth Sciences* **42**, 11–24.

ANDERSON, T. 2002. Correction of common lead in U-Pb analyses that do not report ^{204}Pb. *Chemical Geology* **192**, 59–79.

CANNING, J. C., HENNEY, P. J., MORRISON, M. A. & GASKARTH, J. W. 1996. Geochemistry of late Caledonian minettes from Northern Britain: implications for the Caledonian sub-continental lithospheric mantle. *Mineralogical Magazine* **60**, 221–36.

CHEN, B., JAHN, B. M. & TIAN, W. 2009. Evolution of the Solonker suture zone: constraints from zircon U-Pb ages, Hf isotopic ratios and whole-rock Nd-Sr isotope compositions of subduction- and collision-related magmas and forearc sediments. *Journal of Asian Earth Sciences* **34**, 245–57.

CHEN, B., JAHN, B. M., WILDE, S. & XU, B. 2000. Two contrasting Paleozoic magmatic belts in northern Inner Mongolia, China: petrogenesis and tectonic implications. *Tectonophysics* **328**, 157–82.

CHEN, B., JAHN, B. M. & ZHAI, M. G. 2003. Sr–Nd isotopic characteristics of the Mesozoic magmatism in the Taihang–Yanshan orogen, North China craton, and implications for Archaean lithosphere thinning. *Journal of the Geological Society, London* **160**, 963–70.

CHEN, D., SUN, J. G., LIANG, S. N., FENG, W., CHANG, Y., CHEN, L. & MEN, L. J. 2008. Sr-Nd isotope characteristics and petrogenesis of dykes from Jinchanggouliang. In *Proceedings of the 9th Chinese Mineral Deposits Meeting* (eds Y. C. Chen, C. J. Xue & C. Q. Zhang), pp. 446–8. Beijing: Geological publishing house (in Chinese).

CHEN, J. Q., SUN, J. G., PIAO, S. C., ZHAO, J. K. & ZHAI, Y. F. 2005. Genesis and significance of dark dikes in the Jinchanggouliang mine area, Inner Mongolia: evidences from geochemistry of the major and trace elements. *Journal of Jilin University (Earth Science Edition)* **35**, 707–13 (in Chinese with English abstract).

CHEN, B. & ZHAI, M. G. 2003. Geochemistry of late Mesozoic lamprophyre dykes from the Taihang Mountains, north China, and implications for the sub-continental lithospheric mantle. *Geological Magazine* **140**, 87–93.

CHISTYAKOVA, S. & LATYPOV, R. 2008. Fine-scale chemical zonation in small mafic dykes, Kestiö Island, SW Finland. *Geological Magazine* **146**, 485–96.

COPE, T., RITTS, B. D., DARBY, B. J., FILDANI, A. & GRAHAM, S. A. 2005. Late Paleozoic sedimentation on the northern margin of the North China block: implications for regional tectonics and climate change. *International Geology Review* **47**, 270–96.

CURRIE, K. L. & WILLIAMS, P. R. 1993. An Archean calc-alkaline lamprophyre suite, northeastern Yilgarn Block, western Australia. *Lithos* **31**, 33–50.

DAVIS, G. A., XU, B., ZHENG, Y. D. & ZHANG, W. J. 2004. Indonesian extension in the Solonker suture zone: the Sonid Zuoqi core complex, Inner Mongolian, China. *Earth Science Frontiers* **11(3)**, 135–44.

DAVIS, G. A., ZHENG, Y., WANG, C., DARBY, B. J., ZHANG, C. & GEHRELS, G. E. 2001. Mesozoic tectonic evolution of the Yanshan fold and thrust belt, with emphasis on Hebei and Liaoning Provinces, northern China. In *Paleozoic and Mesozoic Tectonic Evolution of Central and Eastern Asia: From continental assembly to intracontinental deformation* (eds M. S. Hendrix & G. A. Davis), pp. 171–97. Geological Society of America, Memoir no. 194.

GAO, S., RUDNICK, R. L., CARLSON, R. W., MCDONOUGH, W. F. & LIU, Y. S. 2002. Re-Os evidence for replacement of ancient mantle lithosphere beneath the North China craton. *Earth and Planetary Science Letters* **198**, 307–22.

HAN, B. F., KAGAMI, H. & LI, H. M. 2004. Age and Nd-Sr isotopic geochemistry of the Guangtoushan alkaline granite, Hebei Province, China: implications for early Mesozoic crust-mantle interaction in North China Block. *Acta Petrologica Sinica* **20**, 1375–88 (in Chinese with English abstract).

HAN, Q. J., SHAO, J. A. & ZHOU, R. 2000. Petrology, geochemistry and petrogenesis of early Mesozoic diorites in Harqin area, Inner-Mongolia. *Acta Petrologica Sinica* **16**, 385–91 (in Chinese with English abstract).

HART, C. J. R., GOLDFRAB, R. J., QIU, Y. M., SNEE, L., MILLER, L. D. & MILLER, M. L. 2002. Gold deposits of the northern margin of the North China Craton: multiple late Paleozoic-Mesozoic mineralizing events. *Mineralium Deposita* **37**, 326–51.

HONG, D. W., HUANG, H. Z., XIAO, Y. J., XU, H. M. & JIN, M. Y. 1995. Permian alkaline granites in central Inner Mongolia and their geodynamic significance. *Acta Geologica Sinica* **8**, 27–39.

HONG, D. W., WANG, S. G., XIE, X. L. & ZHANG, J. S. 2000. Genesis of positive $\varepsilon_{Nd}(t)$ granitoids in the Da Hinggan Mts–Mongolia orogenic belt and continental crust growth. *Earth Science Frontiers* **7**, 441–56 (in Chinese with English abstract).

HOU, G. T., WANG, Y. X. & HARI, K. R. 2010. The Late Triassic and Late Jurassic stress fields and tectonic transmission of North China craton. *Journal of Geodynamics* **50**, 318–24.

HOU, G. T., WANG, C. C., LI, J. H. & QIAN, X. L. 2006. Late Paleoproterozoic extention and paleostress field reconstruction of the North China Craton, *Tectonophysics* **422**, 89–98.

JAHN, B. M. & CONDIE, K. C. 1995. Evolution of the Kaapvaal craton as viewed from geochemical and Sm-Nd isotopic analyses of intracratonic pelites. *Geochimica et Cosmochimica Acta* **59**, 2239–58.

JAHN, B. M., WU, F. Y., LO, C. H. & TSAI, C. H. 1999. Crust-mantle interaction induced by deep subduction of the continental crust: geochemical and Sr-Nd isotopic evidence from post-collisional mafic-ultramafic intrusions of the northern Dabie complex, central China. *Chemical Geology* **157**, 119–46.

JIAN, P., LIU, D. Y., KRÖNER, A., WINDLEY, B. F., SHI, Y. R., ZHANG, W., ZHANG, F. Q., MIAO, L. C., ZHANG, L. Q. & TOMURHUU, D. 2010. Evolution of a Permian intraoceanic arc–trench system in the Solonker suture zone, Central Asian Orogenic Belt, China and Mongolia. *Lithos* **34**, 245–57.

KUSKY, T. M., LI, J. H. & SANTOSH, M. 2007. The Paleoproterozoic north Hebei orogen: North China craton's collisional suture with Columbia supercontinent. *Gondwana Research* **12**, 4–28.

KUSKY, T. M., WINDLEY, B. F. & ZHAI, M. G. 2007*a*. Tectonic evolution of the North China Block: from orogen to craton to orogen. In *Mesozoic Sub-Continental Lithospheric Thinning Under Eastern Asia* (eds M. G. Zhai, B. F. Windley, T. M. Kusky & Q. R. Meng), pp. 1–34. Geological Society of London, Special Publication no. 280.

Kusky, T. M., Windley, B. F. & Zhai, M. G. 2007*b*. Lithospheric thinning in eastern Asia; constraints, evolution, and tests of models. In *Mesozoic Sub-Continental Lithospheric Thinning Under Eastern Asia* (eds M. G. Zhai, B. F. Windley, T. M. Kusky & Q. R. Meng), pp. 331–43. Geological Society of London, Special Publication no. 280.

Liégeois, J. 1998. Preface – Some words on the post-collisional magmatism. *Lithos* **45**, xv–xvii.

Lin, B. Q., Shang, L., Shen, E. S., Zhang, L. D., Taylor, B. E., Robert, F., Mortersen, J. K. & Poulsen, K. H. 1993. Vein gold deposits of the Liaoxi Uplift, North China Platform. In *Proceedings of the Eighth Quadrennial IAGOD Symposium* (ed. Y. T. Maurice), pp. 597–612. Ottawa: E. Schweizerbart'sche Verlagsbuchhandlung, Science Publishers.

Liu, Y. S., Gao, S., Hu, Z. C., Gao, C. G., Zong, K. Q. & Wang, D. B. 2010. Continental and oceanic crust recycling-induced melt–peridotite interactions in the Trans-North China Orogen: U–Pb dating, Hf isotopes and trace elements in zircons from mantle xenoliths. *Journal of Petrology* **51**, 537–71.

Liu, S., Hu, R. Z., Gao, S., Feng, C. X., Qi, L., Zhong, H., Xiao, T. F., Qi, Y. Q., Wang, T. & Coulson, I. M. 2008*a*. Zircon U–Pb geochronology and major, trace elemental and Sr–Nd–Pb isotopic geochemistry of mafic dykes in western Shandong Province, east China: constrains on their petrogenesis and geodynamic significance. *Chemical Geology* **255**, 329–45.

Liu, D., Nutman, A. P., Compston, W., Wu, J. & Shen, Q. 1992. Remnants of 3800 Ma crust in the Chinese part of the Sino-Korean craton. *Geology* **20**, 339–42.

Liu, Y. S., Zong, K. Q., Kelemen, P. B. & Gao, S. 2008*b*. Geochemistry and magmatic history of eclogites and ultramafic rocks from the Chinese continental scientific drill hole: subduction and ultrahigh-pressure metamorphism of lower crustal cumulates. *Chemical Geology* **247**, 133–53.

Ludwig, K. R. 2003. *User's manual for ISOPLOT 3.00: A Geochronological Toolkit for Microsoft Excel.* Berkeley Geochronology Center Special Publication no. 4.

Lugmair, G. W. & Marti, K. 1978. Lunar initial ^{134}Nd/^{144}Nd: differential evolution of the lunar crust and mantle. *Earth and Planetary Science Letters* **39**, 349–57.

Luo, Z. H., Wei, Y., Xin, H. T., Zhan, H. M., Ke, S. & Li, W. T. 2006. Petrogenesis of the post orogenic dike complex – constraints to lithosphere delamination. *Acta Petrologica Sinica* **22**, 1672–84 (in Chinese with English abstract).

Mayborn, K. R., Lesher, C. E. & Connelly, J. N. 2008. Geochemical constraints on the late-stage evolution of basaltic magma as revealed by composite dikes within the Kangamiut dike swarm, West Greenland. *Lithos* **104**, 428–38.

Menzies, M., Xu, Y. G., Zhang, H. F. & Fan, W. M. 2007. Integration of geology, geophysics and geochemistry: a key to understanding the North China Craton. *Lithos* **96**, 1–21.

Miao, L. C., Fan, W. M., Liu, D. Y., Zhang, F. Q., Shi, Y. R. & Guo, F. 2008. Geochronology and geochemistry of the Hegenshan ophiolitic complex: implications for late-stage tectonic evolution of the Inner Mongolia-Daxinganling Orogenic Belt, China. *Journal of Asia Earth Science* **32**, 348–70.

Miao, L. C., Fan, W. M., Qiu, Y. M., McNaughton, N. J. & Groves, D. I. 2003. Zircon SHRIMP U-Pb geochronology of the granitoid intrusions from Jinchanggouliang-Erdaogou gold orefield and its significance. *Acta Petrologica Sinica* **19**, 71–80 (in Chinese with English abstract).

Miao, L., Zhang, F., Fan, W. & Liu, D. 2007. Phanerozoic evolution of the Inner Mongolia-Daxinganling orogenic belt in North China: constraints from geochronology of ophiolites and associated formations. In *Mesozoic Sub-Continental Lithospheric Thinning Under Eastern Asia* (eds M. G. Zhai, B. F. Windley, T. M. Kusky & Q. R. Meng), pp. 223–237. Geological Society of London, Special Publication no. 280.

Mu, B. L., Shao, J. A., Chu, Z. Y., Yan, G. H. & Qiao, G. S. 2001. Sm-Nd age and Sr, Nd isotopic characteristics of the Fanshan potassic alkaline ultramafite-syenite complex in Hebei Province, China. *Acta Petrologica Sinica* **17**, 358–65 (in Chinese with English abstract).

Müller, D., Rock, N. M. S. Groves, D. I. 1992. Geochemical discrimination between shoshonitic and potassic volcanic rocks in different tectonic settings: a plot study. *Mineralogy and Petrology* **46**, 259–89.

Ni, Z. Y., Zhai, M. G., Wang, R. M. & Tong, Y. 2006. Late Paleozoic retrograded eclogites from within the northern margin of the North China Craton: evidence for subduction of the Paleo-Asian Ocean. *Gondwana Research* **9**, 209–24.

Pearce, J. A. 1982. Trace element characteristic of lavas from destructive plate boundaries. In *Andesites: Orogenic Andesites and Related Rocks* (ed. R. S. Thorpe), pp. 528–48. New York: Wiley.

Pe-Piper, G., Piper, D. J. W., Koukouvelas, I., Dolansky, L. M. & Kokkalas, S. 2009. Postorogenic shoshonitic rocks and their origin by melting underplated basalts: the Miocene of Limnos, Greece. *Geological Society of America Bulletin* **121**, 39–54.

Prelevic, D., Foley, S. F., Cvetkovi, V. & Romer, R. L. 2004. Origin of minette by mixing of lamproite and dacite magmas in Veliki Majdan, Serbia. *Journal of Petrology* **45**, 759–92.

Rapp, R. P. & Watson, E. B. 1995. Dehydration melting of metabasalt at 8–32 kbar: implications for continental growth and crust-mantle recycling. *Journal of Petrology* **36**, 891–931.

Rudnick, R. L. & Fountain, D. M. 1995. Nature and compositions of the continental crust: a lower crustal perspective. *Reviews of Geophysics* **33**, 267–309.

Rudnick, R. L., Gao, S., Ling, W. L., Liu, Y. S. & McDonough, W. F. 2004. Petrology and geochemistry of spinel peridotite xenoliths from Hannuoba and Qixia, North China craton. *Lithos* **77**, 609–37.

Scarrow, J. H., Leat, P. T., Wareham, C. D. & Millar, I. L. 1998. Geochemistry of mafic dykes in the Antarctic Peninsula continental-margin batholith: a record of arc evolution. *Contributions to Mineralogy and Petrology* **131**, 289–305.

Shang, Q. H. 2004. Occurrences of Permian radiolarians in central and eastern Nei Mongol (Inner Mongolia) and their geological significance to the Northern China Orogen. *Chinese Science Bulletin* **49**, 2613–19.

Shao, J. A. 1991. *Crust Evolution in the Middle Part of the Northern Margin of Sino-Korean Plate*. Beijing: Publishing House of Peking University, 138 pp. (in Chinese with English abstract).

Shao, J., Han, Q. & Li, H. 2000. Discovery of the early Mesozoic granulite xenoliths in North China Craton. *Science in China Series D: Earth Science:* **43**, 245–52.

Shao, J. A., Han, Q. J., Zhang, L. Q. & Mu, B. L. 1999. Cumulate complex xenoliths in the early Mesozoic in eastern Inner Mongolia. *Chinese Science Bulletin* **44**, 1272–9.

SHAO, J. A., ZHANG, R. H., HAN, Q. J., ZHANG, L. Q., QIAO, G. S. & SHANG, H. Q. 2000. Geochronology of cumulate xenoliths and their host diorites from Harqin, eastern Nei Mongol. *Geochimica* **29**, 331–6 (in Chinese with English abstract).

SHAO, J. A., ZHANG, Y. B., ZHANG, L. Q., WANG, P. Y. & GUO, F. 2003. Early Mesozoic dike swarms of carbonatites and lamprophyres in Datong area. *Acta Petrologica Sinica* **19**, 93–104 (in Chinese with English abstract).

SHE, H. Q., WANG, Y. W., LI, Q. H., ZHANG, D. Q., FENG, C. Y. & LI, D. X. 2006. The mafic granulite xenoliths and its implications to mineralization in Chaihulanzi gold deposit, Inner Mongolia, China. *Acta Geologica Sinica* **80**, 863–75 (in Chinese with English abstract).

SHE, H. Q., XU, G. Z., ZHOU, R., WANG, Y. F., YAN, D. P., YANG, Z. D. & YANG, Y. 2000. Tectonic and magmatic activities in early Mesozoic and their controlling on gold mineralization in Honghuagou gold ore field, Inner Mongolia. *Earth Science – Journal of China University of Geosciences* **12**, 408–16 (in Chinese with English abstract).

STEIGER, R. H. & JÄGER, E. 1977. Subcommission on geochronology: convention on the use of decay constants in geochronology and cosmochronology. *Earth and Planetary Science Letters* **36**, 359–62.

SUN, S. S. & MCDONOUGH, W. F. 1989. Chemical and isotopic systematics of oceanic basalt: implications for mantle composition and processes. In *Magmatism in the Ocean Basins* (eds A. D. Saunders & M. J. Norry), pp. 313–45. Geological Society of London, Special Publication no. 42.

TAN, J., WEI, J. H., GUO, L. L., ZHANG, K. Q., YAO, C. L., LU, J. P. & LI, H. M. 2008. LA-ICP-MS zircon U-Pb dating and phenocryst EPMA of dikes, Guocheng, Jiaodong Peninsula: implications for North China Craton lithosphere evolution. *Science in China Series D: Earth Science* **51**, 1483–500.

TAN, J., WEI, J. H., LI, Y. H., TAN, W. J., GUO, D. Z. & YANG, C. F. 2007. Geochemical characteristics of late Mesozoic dikes, Jiaodong Peninsula, North China Craton: petrogenesis and geodynamic setting. *International Geology Review* **49**, 931–46.

TANG, K. D. 1990. Tectonic development of Paleozoic foldbelts at the northern margin of the Sino–Korean craton. *Tectonics* **9**, 249–60.

THOMPSON, R. N., LEAT, P. T., DICKIN, A. P., MORRISON, M. A., HENDRY, G. L. & GIBSON, S. A. 1990. Strongly potassic mafic magmas from lithospheric mantle source during continental extension and heating: evidence from Miocene minettes of northwest Colorado, U.S.A. *Earth and Planetary Science Letters* **98**, 139–54.

TIAN, W., CHEN, B., LIU, C. Q. & ZHANG, H. F. 2007. Zircon U-Pb age and Hf isotopic composition of the Xiaozhangjiakou ultramafic pluton in northern Hebei. *Acta Petrologica Sinica* **23**, 583–90 (in Chinese with English abstract).

VAUGHAN, A. P. M. 1996. A tectonomagmatic model for the genesis and emplacement of Caledonian calc-alkaline lamprophyres. *Journal of the Geological Society, London* **253**, 613–24.

WAN, T. F. 2004. *Tectonics of China*. Beijing: Geology Publishing House, pp.152–162 (in Chinese with English abstract).

WANG, Z., XU, Z. X. & YANG, F. H. 1989. Geology and genesis of Erdaogou gold deposit, Liaoning Province. *Journal of Changchun University of Earth Science* **19**, 287–97 (in Chinese).

WINCHESTER, J. A. & FLOYD, P. A. 1977. Geochemical discrimination of different magma series and their differentiation products. *Chemical Geology* **20**, 325–43.

WINDLEY, B. F., ALEXEIEV, D., XIAO, W. J., KRÖNER, A. & BADARCH, G. 2007. Tectonic models for accretion of the Central Asian orogenic belt. *Journal of the Geological Society, London* **164**, 31–48.

WU, F. Y., JAHN, B. M., WILDE, S. A., LO, C. H., YUI, T. F., LIN, Q., GE, W. C. & SUN, D. Y. 2003. Highly fractionated I-type granites in NE China (II): isotopic geochemistry and implications for crustal growth in the Phanerozoic. *Lithos* **67**, 191–204.

WU, F. Y., JAHN, B. M., WILDE, S. A. & SUN, D. Y. 2000. Phanerozoic crustal growth: U-Pb and Sr-Nd isotopic evidence from the granites in northeastern China. *Tectonophysics* **328**, 89–113.

WU, F. Y., WALKER, R. J., YANG, Y. H., YUAN, H. L. & YANG, J. H. 2006. The chemical-temporal evolution of lithospheric mantle underlying the North China craton. *Geochimica et Cosmochimica Acta* **70**, 5013–34.

WU, F. Y., XU, Y. G., GAO, S. & ZHENG, J. P. 2008. Lithospheric thinning and destruction of the North China Craton. *Acta Petrologica Sinica* **24**, 1145–74 (in Chinese with English abstract).

XIAO, W. J., WINDLEY, B. F., HAO, J. & ZHAI, M. G. 2003. Accretion leading to collision and the Permian Solonker suture, Inner Mongolia, China: termination of the central Asian orogenic belt. *Tectonics* **22**, 1484–505.

XU, B. & CHEN, B. 1997. Framework and evolution of the middle Paleozoic orogenic belt between Siberian and North China plate in northern Inner Mongolia. *Science in China Series D: Earth Science* **40**, 463–9.

XU, Y. G., LI, H. Y., PANG, C. J. & HE, B. 2009. On the timing and duration of the destruction of the North China craton. *Chinese Science Bulletin* **54**, 3379–96.

XU, X. W., ZHANG, B. L., QIN, K. Z. & CAI, X. P. 2007. Origin of lamprophyres by the mixing of basic and alkaline melts in magma chamber in Beiya area, western Yunnan, China. *Lithos* **99**, 339–62.

YAN, G. H., MU, B. L., XU, B. L., HE, G. Q., TAN, L. K., ZHAO, H., HE, Z. F., ZHANG, R. H. & QIAO, G. S. 1999. Triassic alkaline intrusives in the Yanliao-Yinshan area: their chronology, Sr, Nd and Pb isotopic characteristics and their implication. *Science in China Series D: Earth Science* **42**, 582–7.

YANG, J. H., CHUNG, S. L., ZHAI, M. G. & ZHOU, X. H. 2004. Geochemical and Sr-Nd-Pb isotopic compositions of mafic dikes from the Jiaodong Peninsula, China: evidence for vein-plus-peridotite melting in the lithospheric mantle. *Lithos* **73**, 145–60.

ZHANG, H. F., GOLDSTEIN, S. L., ZHOU, X. H., SUN, M., ZHENG, J. P. & CAI, Y. 2008*a*. Evolution of subcontinental lithospheric mantle beneath eastern China: Re–Os isotopic evidence from mantle xenoliths in Paleozoic kimberlites and Mesozoic basalts. *Contributions to Mineralogy and Petrology* **155**, 271–93.

ZHANG, H. F., SUN, M., ZHOU, X. H., FAN, W. M., ZHAI, M. G. & YIN, J. F. 2002. Mesozoic lithosphere destruction beneath the North China Craton: evidence from major-, trace-element and Sr–Nd–Pb isotope studies of Fangcheng basalts. *Contributions to Mineralogy and Petrology* **144**, 241–53.

ZHANG, H. F., SUN, M., ZHOU, M. F., FAN, W. M., ZHOU, X. H. & ZHAI, M. G. 2004. Highly heterogeneous late Mesozoic lithospheric mantle beneath the North China craton: evidence from Sr–Nd–Pb isotopic systematics of mafic igneous rocks. *Geological Magazine* **141**, 55–62.

ZHANG, H. F. & YANG, Y. H. 2007. Emplacement age and Sr-Nd-Hf isotopic characteristics of the diamondiferous kimberlites from the eastern North China craton. *Acta Petrologica Sinica* **23**, 285–94 (in Chinese with English abstract).

ZHANG, X. H., ZHANG, H. F., TANG, Y. J., WILDE, S. A. & HU, Z. C. 2008*b*. Geochemistry of Permian bimodal volcanic rocks from central Inner Mongolia, North China: implication for tectonic setting and Phanerozoic continental growth in Central Asia Orogenic Belt. *Chemical Geology* **249**, 262–81.

ZHANG, X. H., ZHANG, H. F., ZHAI, M. G., WILDE, S. A. & XIE, L. W. 2009*a*. Geochemistry of Middle Triassic gabbros from northern Liaoning, North China: origin and tectonic implications. *Geological Magazine* **146**, 540–51.

ZHANG, S. H., ZHAO, Y., LIU, X. C., LIU, D. Y., CHEN, F. K., XIE, L. W. & CHEN, H. H. 2009*b*. Late Paleozoic to early Mesozoic mafic–ultramafic complexes from the northern North China Block: constraints on the composition and evolution of the lithospheric mantle. *Lithos* **110**, 229–46.

ZHANG, S. H., ZHAO, Y., SONG, B., HU, J. M., LIU, S. W., YANG, Y. H., CHEN, F. K., & LIU, X. M. 2009*c*. Contrasting Late Carboniferous and Late Permian–Middle Triassic intrusive suites from the northern margin of the North China craton: geochronology, petrogenesis, and tectonic implications. *Geological Society of America Bulletin* **121**, 181–200.

ZHANG, S. H., ZHAO, Y., SONG, B., YANG, Z. Y., HU, J. M. & WU, H. 2007. Carboniferous granitic plutons from the northern margin of the North China block: implications for a late Palaeozoic active continental margin. *Journal of the Geological Society, London* **164**, 451–63.

ZHAO, G. C., WILDE, S. A., CAWOOD, P. A. & SUN, M. 2001. Archaean blocks and their boundaries in the North China craton: lithological, geochemical, structural and P–T path constraints and tectonic evolution. *Precambrian Research* **107**, 45–73.

ZHENG, J. P., GRIFFIN, W. L., O'REILLY, S. Y., LU, F. X., WANG, C. Y., ZHANG, M., WANG, F. Z. & LI, H. M. 2004*a*. 3.6 Ga lower crust in central China: new evidence on the assembly of the North China craton. *Geology* **32**, 229–32.

ZHENG, J. P., GRIFFIN, W. L., O'REILLY, S. Y., LU, F. X., YU, C. M. & LI, H. M. 2004*b*. U-Pb and Hf-isotope analysis of zircons in mafic xenoliths from Fuxian kimberlites: evolution of the lower crust beneath the North China Craton. *Contributions to Mineralogy and Petrology* **148**, 79–103.

ZHENG, J. P. & LU, F. X. 1999. Mantle xenoliths from kimberlites, Shandong and Liaoning: Paleozoic mantle character and its heterogeneity. *Acta Petrologica Sinica* **15**, 65–74 (in Chinese with English abstract).

ZHOU, X. H., YIN, J. F., ZHANG, L. C. & ZHANG, Y. T. 2009. The petrogenesis of late Mesozoic volcanic rock and the contributions from ancient micro-continents: constraints from the zircon U-Pb dating and Sr-Nd-Pb-Hf isotopic systematics. *Earth Science – Journal of China University of Geosciences* **34**, 1–10 (in Chinese with English abstract).

ZHOU, X. H., ZHANG, G. H., YANG, J. H., CHEN, W. J. & SUN, M. 2001. Sr-Nd-Pb isotope mapping of late Mesozoic volcanic rocks across northern margin of North China Craton and implications to geodynamic processes. *Geochimica* **30**, 10–23 (in Chinese with English abstract).

ZINDLER, A. & HART, S. R. 1986. Chemical geodynamics. *Annual Review of Earth and Planetary Sciences* **14**, 493–571.